Underwater Acoustic Localization for Small Submersibles

• •

Navinda Kottege

Autonomous Systems Laboratory, CSIRO ICT Center, 1 Technology Court, Pullenvale, Queensland 4069, Australia
e-mail: navinda.kottege@csiro.au

Uwe R. Zimmer

College of Engineering and Computer Sciences, The Australian National University, Canberra,
Australian Capital Territory 0200, Australia
e-mail: uwe.zimmer@ieee.org

This article discusses the complete processing chain of a high-precision as well as robust underwater localization method. Range and azimuth as well as relative heading are determined for ranges up to 90 m. For ranges up to 10 m the measured precision is 0.05 m for range, 2 deg for direction, and 5 deg for heading of neighboring vehicles. The system is also designed to be deployable in swarms of vehicles as acoustic localization signals are separated by time slots and maximum length sequence (MLS) signatures. The proposed method is based on the consequent exploitation of MLS broadband signal characteristics and the exploration of several methods for each vehicle to estimate ranges, azimuths, and headings of neighboring vehicles. An existing radio-based swarm communication system provides additional support and leads to enhanced measurement precision and interference robustness. The capabilities and limitations of the proposed systems are experimentally determined and discussed. © 2010 Wiley Periodicals, Inc.

1. MOTIVATION

Self-localization of submersibles inside a swarm of identical vehicles requires update rates that are capable of keeping pace with the swarm motions as well as interference robustness and a high degree of accuracy. The broadband signals deployed in this article are selected and tailored to provide an overall high signal-to-noise ratio (SNR) (which is a way to achieve interference robustness), be long enough to warrant sufficient precision, and be short enough for usability at high update rates. Localization as presented here addresses the estimation of distances and angles (denoted *range* and *azimuth*) under which the neighboring vehicles are observed and the estimation of their current *heading*. In a swarm context the authors consider it essential to be able to predict possible and likely motion directions of all neighbors without tracing their position over time—heading estimation allows for this. Individual vehicles in a swarm are assumed to provide the following essential features:

a. *High agility/maneuverability:* Provided here by means of five independent thrusters without control surfaces (Figure 1).

b. *Communication systems:* Provided here by means of a fully distributed and scalable swarm communication system (Schill & Zimmer, 2006).

c. *Localization system:* A means to determine all positions and headings in local swarm neighborhoods (the topic of this article).

Although a number of further features are relevant for practical deployment (e.g., mechanical robustness, hydro-dynamical efficiency), they are not essential for the discussion of the systems presented in this article. On the other hand, the communication system is closely interlinked with the localization system and the high degree of agility enables flexible swarm control while placing high demands on the localization system.

The embedding of the localization system into the swarm communication system provides a number of additional benefits. First, the distributed, synchronized communication scheduler has full control over the occurring communication collisions and in fact uses them to enhance overall efficiency [for details see work by Schill and Zimmer (2006)]. Therefore all potential communication interferences are explicitly planned and known in advance. They can also be avoided altogether while accepting a certain loss in communication efficiency. Second, if the communication system operates on an electromagnetic basis (e.g., long-wave radio), the time of arrival (TOA) differences between the communication packets and the localization signals provide an additional source of information.

System integration aspects that need to be considered include power management and miniaturization of signal processing components as well as projectors and hydrophones. These are aspects of the engineering and development component of the system that are not discussed here. Computational complexity plays an essential role for the real-time deployment of the algorithms in embedded systems. Generic matched filter approaches for range estimation come at a cost of $\mathcal{O}(N^2)$, yet the use of a range tracking method (as introduced in Section 4.6)

Figure 1. Prototypes of Serafina Mk II AUVs.

reduces the effort to $\mathcal{O}(1)$ and thus facilitates practical deployment.

The review of existing approaches in addressing relative localization for multirobot setups in the underwater domain revealed an increasing reliance on intervehicle communication channels and explicit synchronized clock or round-trip, time-based ranging methods. The Woods Hole Oceanographic Institution (WHOI) Micro-Modem, which utilizes narrowband, frequency hopping, and frequency keying methods, has been used in many current research projects (Freitag, Grund, Singh, Partan, Koski, et al., 2005). The most relevant experiment series for this article that deployed the WHOI modem is discussed by Curcio, Leonard, Vaganay, Patrikalakis, Bahr, et al. (2005), in which surface vehicles communicated via acoustic underwater channels while using surface global positioning system (GPS) as "ground truth" reference. Another variant of this series involved two surface vehicles plus one autonomous underwater vehicle (AUV) and is detailed in Bahr's (2009) Ph.D. thesis. Those works do not address the issues raised here (specifically deployability in large swarms), yet they are the closest works in terms of physically experimented, short-range, relative localization systems.

Table I gives a summary of seven real-world underwater multirobot implementations extracted from the literature in reverse chronological order. Given the various platforms, spatial scales of operation, performance metrics used, and different motivations (formation keeping, adaptive sampling, waypoint navigation, etc.), it is extremely difficult to qualitatively compare the performances of different localization techniques. However, *localization sensors* such as those mentioned in the land-based multirobot

Table I. Summary of experimental setups and results extracted from the literature in which the problem of simultaneous navigation of multiple AUVs was addressed.

Number of nodes (type)	Used communication?	Internode distance or survey area	Position errors (reference)
Navigation of multiple AUVs using synchronous clock one-way travel time (Eustice, Whitcomb, Singh, & Grund, 2007)			
2 (1 AUV, 1 ship)	Yes	200×200 m	$\sim$2–5 m (LBL)
Static sensor node networks for AUV localization (Corke, Detweiler, Dunbabin, Hamilton, Rus, et al., 2007)			
5 (4 static, 1 AUV)	Yes	80×80 m	$\sim$2.5 m (GPS)
Coordination and control of an underwater glider fleet (Fiorelli, Leonard, Bhatta, Paley, Bachmayer, et al., 2006)			
3 (gliders)	Yes[a]	3,000–6,000 m	255–623 m (GPS)
Cooperative localization for AUVs using moving baseline navigation (Bahr, 2009; Curcio et al., 2005)			
3 (autonomous kayaks)	Yes	25–100 m	$\sim$1% of range (GPS)
Two-hydrophone heading sensor for multiple AUV navigation (Baker, Odell, Anderson, Bean, & Edwards, 2005)			
2 (1 static, 1 boat)	No[b]	500×500 m	$\sim$10 m (LBL)
Localization and navigation for multiple AUVs using acoustic communication (Stojanovic, Freitag, Leonard, & Newman, 2002)			
3 (2 static, 1 boat/surf zone crawler)	Yes	Up to 2,000 m	$\sim$6 m (GPS)
Multifrequency LBL beacon network for multiple AUV navigation (Cruz, Madureira, Matos, & Pereira, 2001)			
3 (2 static, 1 AUV)	No	$4,000 \times 8,000$ m	$\sim$5–10 m (LBL/inertial)

The position errors are either nominal or average errors explicitly reported by the authors or derived from the provided plots.
[a]Communication with external base station via satellite phone links once at the water surface.
[b]The proposed strategy requires intervehicle communication not used during experiment.

literature (Fox, Burgard, Kruppa, & Thrun, 2000; Howard, Mataric, & Sukhatme, 2003), which provides relative estimates for range, azimuth, and heading of another robot based on observation and sensing, have not been implemented in underwater robotics to address the problem of relative localization to support swarming. Furthermore, a significant body of work addresses distributed underwater control from an information and control theoretical point of view. See, for instance, the work on small glider formation control by Davis, Leonard, and Frantantoni (2009) or large AUV formation control by Kalantar and Zimmer (2009). A common attribute of this literature is that physical experimentation involving a larger school of vehicles with active, distributed swarm coordination that would demonstrate scalability in school size has not yet been performed.

The work presented in this article was motivated by the need for a fully decentralized underwater *localization sensor* capable of delivering instantaneous estimates of relative azimuth, range, and heading of neighboring robots without relying on integration of multiple (angle only or range only) observations to estimate position and heading as done in the target motion analysis literature (Ristic, Arulampalam, & McCarthy, 2002). Although the aim was to develop this system to be implemented on small, Serafina-class AUVs, the availability of such a low-level "sensor" makes it possible to explore the abundant swarm robotics literature to find many candidate high-level cooperative navigation and localization strategies that have been developed and studied over the years that assume the availability of such sensors.

Intermediate findings reported by the authors in previous articles (Kottege & Zimmer, 2007, 2008a, 2008b) are consolidated in this text to provide a more comprehensive description including essential enabling techniques and methodologies. The article continues from here by introducing maximum length sequence (MLS) signals and discussing their characteristics. The overall structure is introduced next (Section 3), followed by a brief explanation of how the proposed system can facilitate distributed localization in a swarm. The required individual methods are specified in Section 4. The rest of this article describes experiments and then presents and discusses results.

2. PROVIDING ROBUSTNESS

The performance of the localization system in the face of interference is provided mainly by the use of an MLS signal as the source ping. A brief introduction to MLS signals is given in the next section, followed by an overview of interference handling strategies utilized in this work.

2.1. Maximum Length Sequences

An MLS is a pseudo-random binary sequence. The statistical properties of these sequences were introduced by Golomb (1982) in his first edition published in 1967. The most attractive of its properties is its autocorrelation function, which is essentially a Dirac delta function (single sharp peak at zero shift).

Acoustically transmitted MLS signals (instead of "0"s and "1"s, these signals consist of −1 and +1) are widely used in fields such as room acoustics to measure the impulse response of linear systems without actually using impulsive signal sources (Borish & Angell, 1983). It has also been shown that the MLS approach yields a higher SNR and better spatial resolution than conventional methods when used for underwater bottom profiling (Farina, 1998).

Although behaving similarly to band-limited white noise in the frequency domain with a quasi-flat spectrum up to the Nyquist frequency, MLS signals have the additional advantage of being fully deterministic. This property makes them accurately reproducible and also provides the ability to have multiple unique signals with the same spectral properties with guaranteed minimal cross correlation among them. These properties combined with the experimental performance makes MLS signals an ideal candidate for the source signal to be used in the relative localization system presented in this article. Section 2.2 gives an evaluation of several broadband source signals including MLS signals in a highly reverberant environment.

There are many standard algorithms for the generation of MLSs by using generating polynomials with different degrees, which results in MLS signal sets of different lengths. The degree n of the generating polynomial, which is also the length of the shift register (also known as the degree of the MLS signal) governs the length l_{MLS} of the sequence as $l_{MLS} = 2^n - 1$. The length of the sequence and the employed sampling rate of the analog-to-digital converter determine the duration of the signal. Even though longer MLS signals give a better resolution of the cross-correlation peak, resulting in higher precision of the consequent estimation, a longer duration has its drawbacks. Owing to undesirable echoes in cluttered or enclosed environments, higher processing overheads, and lower update rate for the overall estimation system associated with a longer duration signal, a relatively short MLS signal of degree 7 (length 127) is employed as a compromise.

2.2. Experimental Evaluation of Alternative Signal Waveforms

Five different types of candidate signal waveforms were experimentally evaluated. These were as follows:

a. An MLS signal of length 127 (as introduced in the preceding section).
b. A chirp with an upsweep of 750–48,000 Hz with a logarithmic chirp rate.
c. A chirp with an upsweep of 750–48,000 Hz with a linear chirp rate.
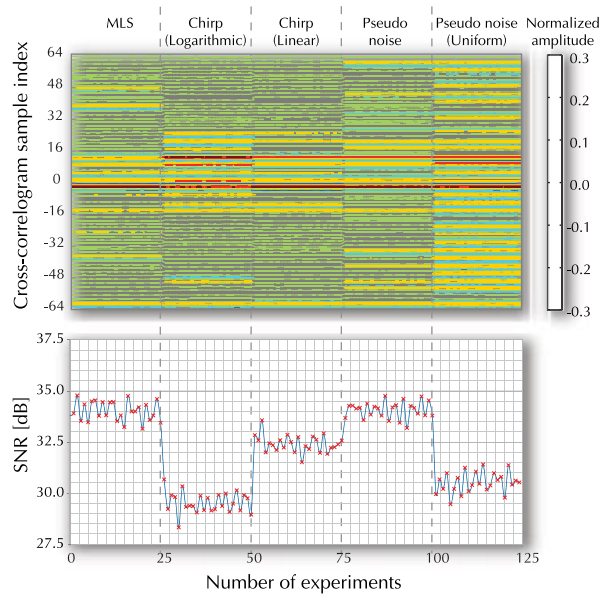
Figure 2. Performance comparison of potential wide-band source signals. Top shows a contour plot depicting the top view of a series of consecutive cross correlograms (25 for each signal type), where the darker areas represent the peak position, and the bottom plot shows the corresponding SNRs.
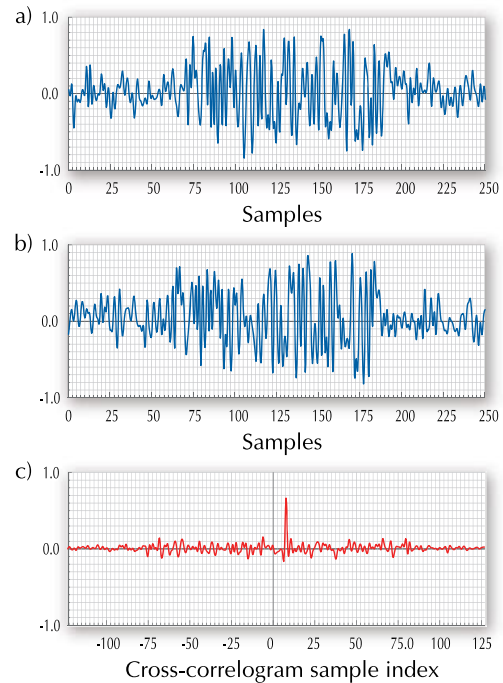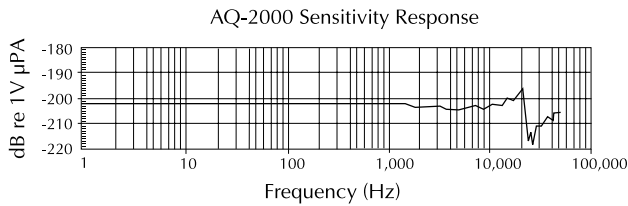

Figure 3. (c) Results from the cross correlation of the shifted noisy MLS signals shown in (a) and (b). In each plot, the y axis represents normalized amplitude.

d. A pseudo-noise signal based on the MT19937 pseudo-random generator.[1]

e. A uniform pseudo-noise signal based on the MT19937 pseudo-random generator.

Amplitudes were normalized and all signals set to an equal length of 127 samples or 1.3 ms. The same projectors, amplifiers, and hydrophones were used in all cases. The test environment constitutes an enclosed reverberant metal tank of 4.2-m diameter and 1.5-m depth. The resulting cross correlograms of 25 averaged test runs per signal as well as the detected SNR are depicted in Figure 2. The MLS signal achieved an equivalent SNR as the pseudo-noise signal, while performing noticeably better than all other remaining signal waveforms. The ability to generate several uncorrelated MLS signals of identical lengths is an advantage of the MLS signal, which does not become apparent in this measurement yet will become important in the further discussion.

2.3. Effect of Uncorrelated Noise

The robustness of MLS signals against uncorrelated noise, even at relatively short lengths, is demonstrated as follows.

Two copies of the MLS signal are used, where one is shifted by eight samples, such that the first channel leads. Then the two signals are contaminated with additive white Gaussian noise and cross correlated. The average signal powers were equal [−3 dB full scale (dBFS)] when mixing white noise with the MLS signal representing a SNR of 0 dB. The two signals [plots (a) and (b)] and the resulting cross correlogram [plot (c)] are shown in Figure 3. The position and width of the peak of the cross correlation as well as the area surrounding the peak remain unaltered in this case. However, the height of the peak has been reduced to about 70% of its original value compared to the autocorrelation function.[2]

2.4. Effect of Nonlinear Transducers

As was shown by Figure 3(c), contamination by additive white noise does not contribute to a noticeable deterioration of the cross-correlation performance of MLS signals, apart from a lower height for the peak. In theory, the addition of two "flat" frequency spectra should again result in a "flat" frequency spectrum; hence the spectral properties of the MLS signal that provide the narrowness of the peak are preserved. However, this is not necessarily the

---

[1]Implementation of the Mersenne Twister pseudo-random generator is given by Hoe (2002), and the theory behind the implementation is given by Matsumoto and Nishimura (1998).

[2]See work by Kottege (2009, pp. 51–52) for a more detailed discussion of this observation.

Figure 4. The frequency response curve of the hydrophone reproduced from the AQ-2000 data sheet.

Figure 5. Cross-correlogram plots resulting from (a) unfiltered signal channels and (b) filtered signal channels, showing the main peak and adjacent side-lobe peaks. The *y* axes represents the normalized amplitude.

case when these signals are transmitted and received via transducers with a nonlinear frequency response within the bandwidth of the signal. Owing to the sampling rate used ($f_s = 96$ kHz), the signals are band limited by 48 kHz. The frequency response of the Benthos AQ-2000 transducers, which are used as transmitting projectors as well as receiving hydrophones, is shown in Figure 4. As seen from this plot, the transducers have a resonance near 20 kHz and an antiresonance near 25 kHz, which result in a highly nonlinear response within the signal bandwidth leading to multiple side-lobe peaks in the vicinity of the cross-correlogram peak. To circumvent this effect, an inverse frequency response filtering scheme is used.[3] Figure 5 shows the results of this technique. As depicted, applying the filter results in the uniqueness and narrowness of the peak being restored, making it possible to unambiguously locate it.

3. STRUCTURE AND COMPONENTS

This system draws insights from hyperbolic and spherical positioning schemes (Deffenbaugh, Bellingham, & Schmidt, 1996) and provides each vehicle with a regularly updated pose vector (consisting of the azimuth, range, and heading) of its near neighbors with respect to its own frame of reference. As opposed to most relative localization schemes described in the literature, which treat swarm members as point objects and hence provide no heading direction (apart from integrating multiple position updates), this explicitly estimates the heading direction and is included in the pose vector with each update. The implementation utilizes an acoustically transmitted MLS signal from projectors on the bow (front) and stern (rear) ends of each "sender" vehicle, which in turn is received by a pair of hydrophones on the "observer" vehicles at each update cycle. The statistical properties of the MLS signals provide extremely high robustness against interference by multipath arrivals, cross-talk and noise sources, and other inherent detrimental effects in the underwater environment as well as the nonlinear characteristics of the transducers used.

Whereas the azimuth is obtained via hyperbolic positioning techniques measuring multiple time difference of
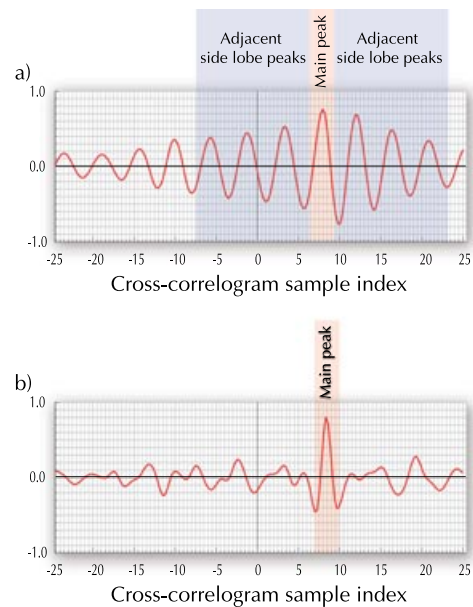
arrivals (TDOAs) between the hydrophones, the resolution and accuracy is greatly improved over those achieved by conventional methods using effective outlier handling schemes. The range and heading estimation is performed utilizing two independent methods that are assumed to provide higher reliability and robustness in a fast-changing and dynamic environment. One method uses the implicit synchronization provided by the underlying scheduling system developed by Schill and Zimmer (2007) to measure the difference of TOAs of the acoustic and electromagnetic (long-wave radio) signals. This gives an equivalent measure to the time of flight (TOF) of the acoustic signal, which is converted to a distance as done in spherical positioning schemes. The alternate method, which relies only on multiple TDOAs and sensor geometry, estimates the range without any explicit knowledge of the sending times of the acoustic signals or reliance on the synchrony provided by the communication and scheduling system. The reverse hyperbolic estimation scheme used here provides a safeguard against erroneous range and heading estimation due to loss or drift of synchronization between the neighboring vehicles.

3.1. System Overview

The block diagram in Figure 6 gives the functional components of the relative localization system while depicting the flow of information from the acoustic pings received by

---

[3]See work by Kottege (2009, pp. 53–57) for more details.
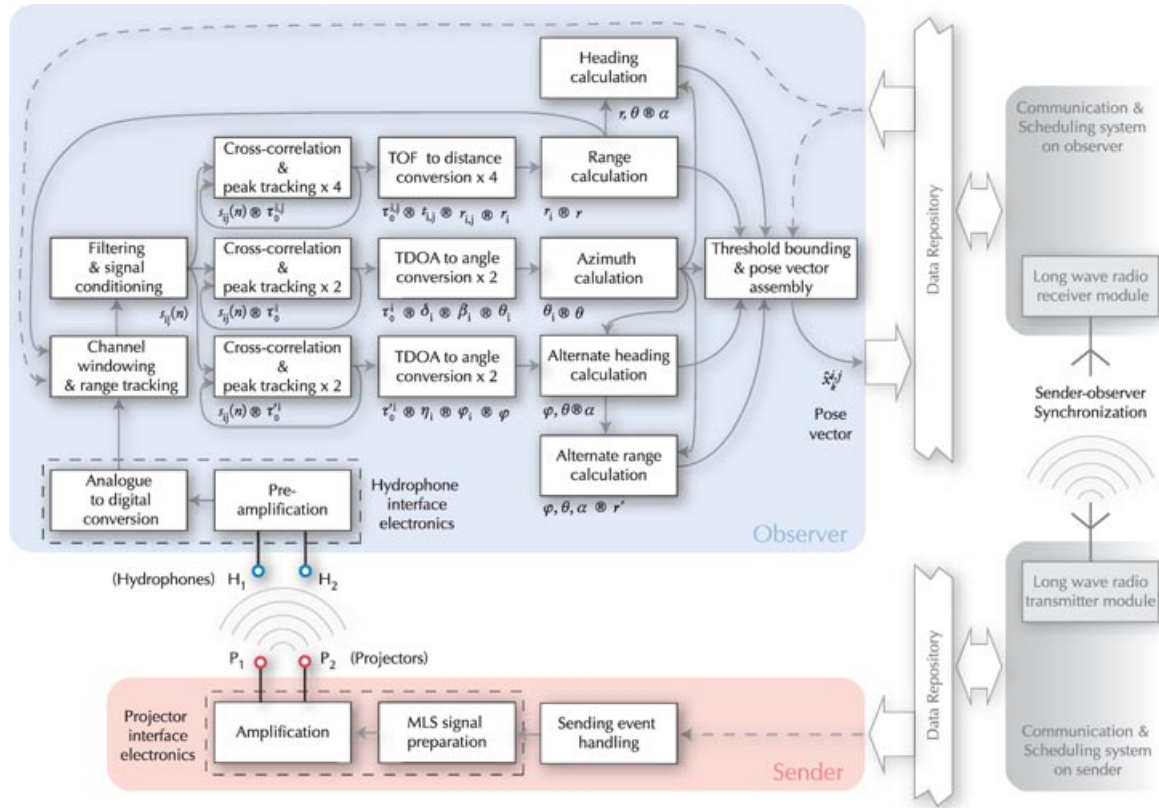
Figure 6. Block diagram showing main modules and components of the relative localization system.

the hydrophones to the final pose vector assembly. Specific hardware and software modules used in the experimental implementation of the system are described in Section 5, and overviews of the main components of the information flow are given in the following sections.

3.1.1. Acoustic Signal Reception and Preparation

The main external inputs to the system are provided via the hydrophones, which receive the MLS pings transmitted by the sender. Once in digital form, the channels are "windowed" into finite-length segments. The length of the channel window in sample space is related to the sampling frequency of the analog-to-digital converters, the speed of sound underwater, the sample length of the MLS ping, and the maximum effective range of the localization system, introduced in Section 3.2.1. This length can be given as

$$N = r_{\max}(f_s/v) + l_{\mathrm{MLS}}. \tag{1}$$

The two separate pings emitted by projectors P_1 and P_2 of the sender, which constitute a sending event, are separated in time by t_{FB} to avoid interference. Therefore, the channel windowing module assembles two length-N signal segments, each with two channels corresponding to the

two hydrophones H_1 and H_2. The start of a sending event is signaled to the channel windowing module via the long-wave radio receiver module (events simulated in all experiments presented in this article), which is part of the communication and scheduling system residing on the observer, as soon as it receives a message from a sender. Therefore, the beginning of the first windowed segment is aligned with the start of the sending event, which resets a sample counter. The beginning of the second segment is aligned with sample $t_{\mathrm{FB}} f_s + l_{\mathrm{MLS}}$. To overcome the computational cost of range estimation for longer ranges, a range tracking scheme is introduced in Section 4.6.3. Here, the channel segments are further cropped based on the previous range estimates related to a particular sender.

The two channels of the first segment (ping emitted by P_1) are denoted by $s_{11}(n)$ and $s_{12}(n)$, and the two channels of the second segment (ping emitted by P_2) are denoted by $s_{21}(n)$ and $s_{22}(n)$. Once assembled, these are filtered with the frequency filter introduced in Section 4.6. This is done by transforming the signals into the frequency domain using a fast Fourier transform (FFT), multiplying with the response of the filter and then transforming back into the sample domain using an inverse FFT. These channels serve as inputs to the subsequent cross correlations,

which derive the TDOAs and TOFs used for the pose vector estimation.

3.1.2. TDOA and TOF Measurements

As depicted in Figure 6, the cross correlations for deriving the TOFs for range estimations and TDOAs for azimuth and alternate heading estimations are processed in parallel. The peak tracking scheme, which is presented in Section 4.6.1. operates at a very low level in the processing chain, utilizing the information about the peak positions of cross correlograms derived in the previous estimation step.

3.1.3. Localization Estimates and Pose Vector

Once TDOA and TOF readings are identified, the pose vector components azimuth θ, range r, and heading α along with alternate heading and range are calculated and assembled into a pose vector. Out of these, azimuth, range, and alternate heading are categorized as primary estimates. Quantities that are derived from these primary estimates, namely the heading and alternate range, are categorized as secondary estimates. Outliers resulting from the numerical instability of formulas used to derive these secondary estimates in certain physical configurations are handled with the threshold bounding scheme (described in Section 4.6.2).

Each of the assembled pose vectors is attributed with the node IDs of the sender vehicles provided via the communication and scheduling system residing on the observer. For an observer AUV with node ID j that receives acoustic pings after an AUV with node ID i initiates a sending event, corresponding to a logical time step[4] k, the pose vector $x_k^{i,j}$ is expressed as $[\theta, r, \alpha]^T$ for $k \in \mathbb{N}$ and $i, j = 1, 2, \ldots N_0, i \neq j$, with N_0 being the total number of vehicles in the swarm.

3.2. Distributed Relative Localization

The block diagram in Figure 6 depicted only one sender and one observer, as this was sufficient to describe the process of relative localization to be used by individual AUVs. However, it was elucidated that for each sending event initiated by a sender, multiple observers within its local neighborhood can localize it. Furthermore, multiple simultaneous sending events can occur within a swarm, depending on the structure of the distributed omnicast routing schedule used by the underlying long-wave radio communication system (Schill, 2007).
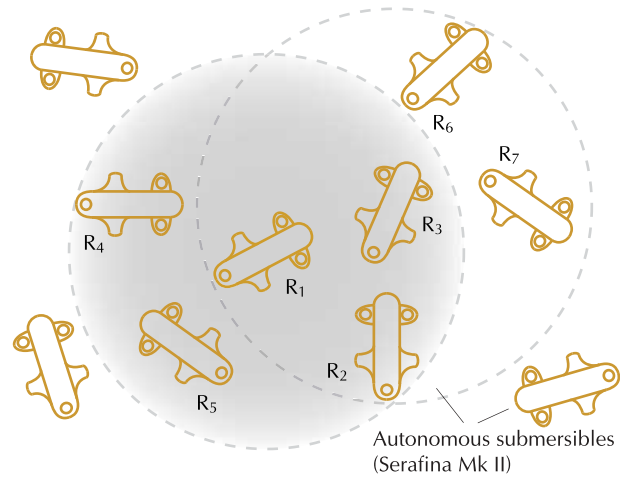
Figure 7. AUVs labeled R_2, R_3, R_4, and R_5 receive the acoustic signals when the "sending" vehicle R_1 is within their sensing range. The four vehicles that receive the signals sent out by R_1 constitute its local neighborhood. When R_3 is "sending," R_1, R_2, R_6, and R_7 make up the local neighborhood of R_3. The number of vehicles in a local neighborhood depends on the swarm density and the range of the localization system.

The simplified diagram[5] given in Figure 7 can be used to explain the concept of a local neighborhood with regard to an acoustic sending event. As the AUV labeled R_1 is "sending," vehicles R_2, R_3, R_4, and R_5, which have it within their sensing range, would be able to receive the acoustic signals. In this case, the four vehicles that receive the signals sent out by R_1 constitute its local neighborhood. Similarly when R_3 is "sending," R_1, R_2, R_6, and R_7 make up its neighborhood. Assuming that a large swarm consists of many such local neighborhoods, the time division multiple access (TDMA) scheduling scheme allows multiple sending events to occur simultaneously (Schill, Zimmer, & Trumpf, 2005; Somaraju & Schill, 2007). Within one schedule run, each member of the swarm would have information about the relative positions of each of its neighborhood members via the relative localization system.

Whereas a given sending event allows multiple observers to fix the static position of a sender, the time history of pose vectors (corresponding to that particular sender) would describe the relative motion of the vehicle with respect to the frame fixed on each of the observers. Furthermore, at each sending event, the sender is meant to broadcast (via the long-wave radio communication system, within the local neighborhood of the sender) the pose vectors estimated thus far within the scheduling run. Therefore, at the end of each local schedule run, each member of

---

[4]Logical time is not necessarily related to a real-time clock, as explained by Lamport (1978).

[5]Although the diagram depicts the sending range of an AUV as a circle, in practice it is a more complex shape depending on transducer directivity and occlusion effects.

a local neighborhood would have position fixes for all its neighbors obtained directly from the localization system as well as the pose vectors assembled by all other neighbors via the communication system. The position data received via multiple methods along with proprioceptive measurements from other systems such as the inertial measurement unit (IMU), magnetic compass, and pressure sensor onboard the Serafina-class AUVs will serve as inputs to a "higher level" system[6] to perform cooperative localization within the swarm.

3.2.1. Update Rates

Multiple update rates operating at different levels can be identified with regard to distributed localization in a swarm in which the lowest level is the rate at which the pose vector is updated by a particular observer vehicle: that is, how often a vehicle would be able to get a position fix of some other vehicle in the local neighborhood. This depends on the duration of a schedule slot (logical time step). The possible duration of the time step has a lower bound introduced by the effective sensing range of the localization system, which is equivalent to the maximum radius of a local neighborhood. If the time-step duration is t_{TS} and the maximum effective sensing range of the localization system is r_{max}, this constraint based on the composition of a sending event that includes two send–receive cycles can be expressed as

$$t_{TS} \geq t_R = \frac{2r_{max}}{v}, \qquad (2)$$

where v is the speed of sound in water and t_R is denoted as the receiving time associated with one sending event. Accordingly, the low-level update rate is inversely proportional to the effective sensing range of the relative localization system. Figure 8 illustrates the time line of an observer (R_2) with regard to two sending events initiated in time steps k and $k + 1$ by two senders (R_1 and R_3). The sending time can be expressed as $t_s = 2t_{MLS} + t_{FB}$, where t_{MLS} is the duration of one acoustic ping and t_{FB} is the temporal separation between the two pings.

Another update rate is how often an observer would be able to localize a given sender in its local neighborhood (e.g., according to Figures 7 and 8, how often R_2 can get a position fix for R_1). This would occur at least once in each schedule run. The exact update rate is governed by the structure and the length of the local routing schedule as well as the duration of a schedule slot (same as the logical time step described earlier). The schedule length increases with the number of vehicles in the local neighborhood, whereas the schedule structure is dependent on the spa-
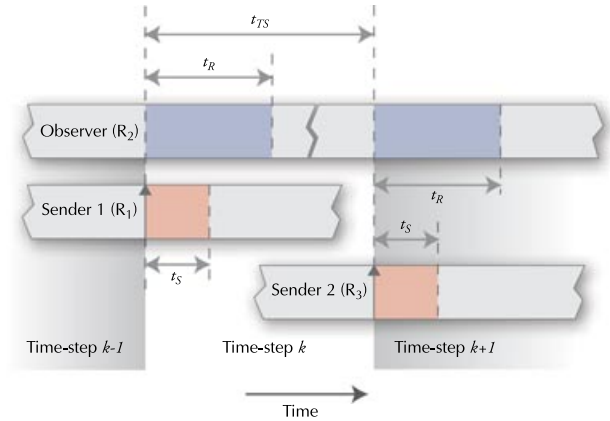
Figure 8. The time line of an observer receiving signals from two sending events initiated by two senders in consecutive schedule slots. The labels R_1, R_2, and R_3 relate to the diagram in Figure 7.

tial configuration of swarm members (e.g., swarm density, shape). This particular update rate is inversely proportional to the number of members in a local neighborhood (due to lengthening of the communication schedule) as well as the effective sensing range of the localization system [due to the relationship between the duration of a schedule slot and effective sensing range given in relation (2)].

3.2.2. Sensing Range

The requirement is for the acoustic sending to have a range similar to that of the long-wave radio communication. The maximum effective range of the localization system is less than or equal to the maximum range at which the SNR of the acoustic signals still provide acceptable localization estimates within error bounds. The maximum range is dependent on a number of external parameters such as the sensitivity of the hydrophones used, the transmission power of the acoustic pings, the preamplifiers, and the dynamic range of the analog-to-digital converters. However, the effective range of the localization system is related to the length N of the truncating window applied to the received signal channels.

3.2.3. Relationship between Effective Sensing Range and the Update Rate

As mentioned earlier, incoming acoustic channels are windowed into two length-N segments, each containing a ping emitted within the sending event. The window length determines the maximum distance traveled by the acoustic signal before reaching the hydrophones. This in turn is the maximum effective sensing range r_{max} of the system that is related to N according to Eq. (1). However, the time delay t_{FB} separating the two pings emitted during a sending

---

[6]A detailed description of how this high-level localization system is to be realized for Serafina-class AUVs is beyond the scope of this work.

event imposes an upper limit on the maximum detectable range given as

$$r_{\max} \leq v t_{\text{FB}}, \tag{3}$$

where the speed of sound in water v is in meters per second, t_{FB} is in seconds, and $r_{\max}$ is in meters.

Furthermore, the duration t_{FB} also dictates the maximum achievable low-level update rate for the system mentioned at the beginning of Section 3.2.1. Considering Eq. (1) and relation (2), the maximum low-level update rate for the system has an upper bound based on and that can be expressed as

$$u_{\max} \leq \frac{1}{2(t_{\text{FB}} + t_{\text{MLS}})}, \tag{4}$$

with $t_{\text{MLS}} = l_{\text{MLS}}/f_{\text{s}}$, where l_{MLS} is the sample length of an MLS ping and f_{s} the sampling frequency of the analog-to-digital converters. The update rate is in hertz, when t_{FB} is in seconds and f_{s} is also in hertz, whereas l_{MLS} is unitless, given in sample points.

The upper bounds for $r_{\max}$ and $u_{\max}$ are plotted against t_{FB} in Figure 9. The vertical dashed line on the plot represents the t_{FB} value used in the experiments presented in the following section, which is 5.0×10^{-2} s. For this value, relations (3) and (4) suggest a maximum low-level update rate of 9.74 Hz and a maximum detectable range of 75 m. The update rate actually used during the experiments was 5.0 Hz. Considering the upper bounds plotted in Figure 9, the optimal value for the time delay t_{FB} suggested by the plot is 1.74×10^{-2} s, the corresponding maximum update rate is 26.4 Hz, and the maximum detectable range is 26.4 m.
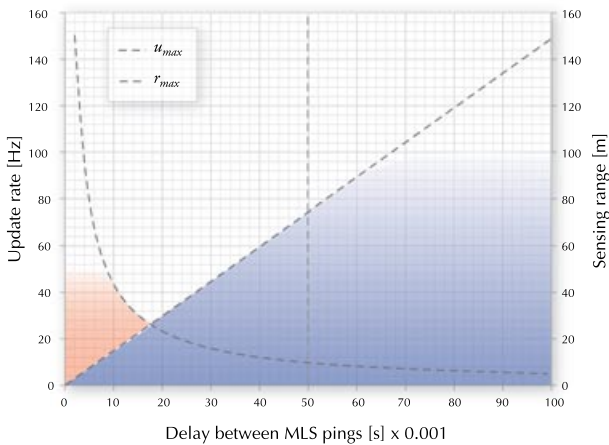
The upper bounds suggested by the plot depict theoretical limits and will be reduced in any practical deployment due to multiple reasons. To reach the linearly increasing maximum ranges suggested, the transmission power needs to be increased accordingly, as the deterioration of the SNR is not considered by relation (3). The maximum detectable range is limited in practice by multipath propagation and attenuation of the underwater sound channel. Hence only parts of the area underneath the dotted line in Figure 9 can be utilized. A detailed analysis of these limitations will require an extensive series of experiments in many different environments and is currently outside the scope of this work. Furthermore, the maximum update rate will be limited at an upper bound depending on the processor used by the system. This limiting level is represented by the shading of the plot as opposed to the exponential increase suggested by relation (4).

Depending on how reverberant the operating environment is, t_{FB} cannot be reduced below a threshold value. This threshold needs to be determined for each class of environments and will ensure that all the echoes and reflections of the first ping have sufficiently attenuated[7] before the start of the second. The value selected for t_{FB} dictates the maximum low-level update rate and maximum detectable range of the system. However, the range tracking strategy described in Section 4.6.3 eliminates the constraint on the maximum effective range imposed by relation (3) based on t_{FB}.

4. METHODOLOGY

The following sections describe and define the methods used to calculate the angles and distances used to derive the localization estimates, their measuring conventions, and the geometric relationships.

4.1. Azimuth Estimation

Figure 10 depicts a source at P_1 and two receivers at H_1 and H_2. The signal from P_1 takes two different paths to reach H_1 and H_2, traversing path lengths of r_{11} and r_{12}, respectively (Piersol, 1981). This difference in path lengths can be defined as $\delta = r_{11} - r_{12}$. With the spacing between the receivers denoted by d and following the standard definition of a hyperbola, the locus of P_1 can be defined as lying on a branch of a hyperbola with its foci at H_1, H_2 and eccentricity $d/|\delta|$. Considering the polar coordinates of P_1 as (r_1, β), where the polar axis lies along $H_1 H_2$ with the pole at O_1, the angle of arrival of a signal originating from P_1 (located sufficiently far away compared to the spacing between the

Figure 9. Maximum theoretically achievable update rate and detectable range $r_{\max}$ plotted against the delay between the two MLS pings within a sending event.

---

[7]Empirical evidence from the experiments conducted in the test tank suggests that an attenuation of 20 dB is sufficient.
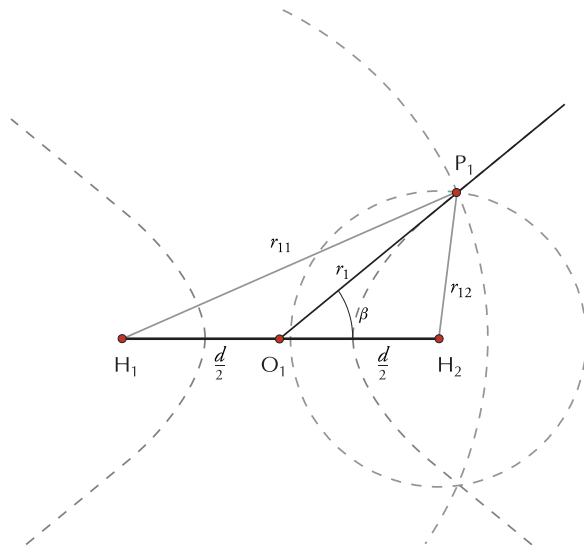
Figure 10. Intersecting two circles centered at H_1 and H_2 with the line defining angle of arrival of the signal uniquely localizing the source position P_1.

receivers[8]) can be given as

$$\beta = \pm \tan^{-1} \left(\frac{\sqrt{d^2 - \delta^2}}{\delta} \right), \tag{5}$$

where β is the gradient of the asymptotes of the hyperbola.

As can be inferred from Figure 10 as well as Eq. (5), the path length difference δ varies between $-d$ and $+d$. The sign of δ determines which branch of the hyperbola contains P_1. However, a given value of δ yielding a value for β still holds an ambiguity, referred to as the *front–back ambiguity*. Any location of P_1 and its reflection about $H_1 H_2$ would give the same path length difference. The $\pm$ sign in Eq. (5) represents this ambiguity. In the absence of extra information from additional sensors, omnidirectional receivers cannot usually resolve this ambiguity. The relative localization system presented in this article uses non-omni-directional hydrophones as receivers and consequently avoids this problem although being limited in angular coverage.[9] Therefore, the $\pm$ sign will be dropped from the formulas in the subsequent discussions. Furthermore, the signal source is assumed to be on the same plane containing the two receivers and their main axes of directivity. However, the principle of path length difference extends to the third dimension, where the source lies outside the aforementioned plane. In this case, the branches of the hyperbola are replaced by sheets of a three-dimensional hy-

[8]In practice, this condition is satisfied when $r_1 > 2d$.
[9]The actually measured direction sensitivity is documented in Section 5.

perboloid and the asymptote lines are replaced by cones. Strategies for extending the localization system into the third dimension by fusing additional sensor information (relative depth) and utilizing additional hydrophones are proposed and experimentally validated in work presented by Kottege (2009, pp. 205–216).

Whereas the path length difference described earlier is given as a distance, the speed of propagation of the signal relates it to a time delay t_D referred to as the TDOA given by $t_D = \delta/v$, where v is the speed of propagation of the source signal.

An estimate for t_D can be given as the argument τ that maximizes the continuous-time representation of the cross-correlation function of the time-domain signals $s_1(t)$ and $s_2(t)$ received via H_1 and H_2, respectively (Knapp & Carter, 1976). However, in the relative localization system being discussed, the signals received via the hydrophone channels are two discretely sampled time-series signals of finite length N that can be denoted by $s_1(n)$ and $s_2(n)$. The cross-correlation function of these signals can be expressed as follows:

$$R_{s_1, s_2}(\tau) = \sum_{n=i}^{N-|k|-1} s_1(n) s_2(n - \tau), \tag{6}$$

where $i = \tau$, $k = 0$ for $\tau \geq 0$ and $i = 0$, $k = \tau$ for $\tau < 0$. When considering the full range, which includes both positive and negative lags, the resulting cross-correlation function is of length $2N + 1$ with the sample index spanning $-N$ to $+N$. The sample index τ_0 that corresponds to the TDOA t_D can be expressed as

$$\tau_0 = \arg \max_\tau [R_{s_1, s_2}(\tau)]. \tag{7}$$

Then $t_D = \tau_0/f_s$, where f_s is the sampling frequency of the analog-to-digital converters used. To measure the angle of arrival of the signal using Eq. (5), τ_0 is related to δ as

$$\delta = \tau_0 v / f_s. \tag{8}$$

Figure 11 shows the mounting configuration of hydrophones and projectors on the hull of a Serafina Mk II–class AUV and how it corresponds with the sender and receiver positions P_1, P_2 and H_1, H_2. The hydrophone spacing d is set to 0.3 m, and the projector spacing l is set to 0.5 m, based on the physical size of the AUV hull. The pole of the coordinate frame O lies at the intersection of two lines $H_1 H_2$ and $P_1 P_2$ coinciding with the center of buoyancy of the AUV. The polar axis is along the centerline of the AUV, which goes through the projectors P_1 and P_2 and points toward the bow end of the vehicle.

Figure 12 illustrates AUV labeled R_1 (observer) measuring the azimuth, range, and heading of AUV R_2 (sender). These relative measurements are based on a polar coordinate system fixed on R_1 with its pole at O_1. Figure 13 shows a geometric abstraction of two vehicles, the sender with its two projectors P_1 and P_2 and the observer
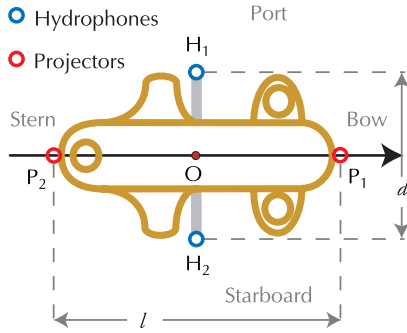
Figure 11. Hydrophones H_1 and H_2 are positioned on the port and starboard sides, and projectors P_1 and P_2 are positioned on the bow and stern ends of Serafina AUV hulls. The diagram illustrates a top view.

with its two hydrophones H_1 and H_2. O_1 and O_2 represent the poles of the body fixed polar coordinate frames of the observer and the sender, respectively. The azimuth θ is defined as the angle between the polar axis going through O_1 and the line O_1O_2. This quantity, with a range of -180 deg $< \theta < +180$ deg, is measured as positive clockwise and as negative counterclockwise from the polar axis.

The angle measurement using TDOA gives β_1 and β_2, corresponding to the angles that the lines P_1O_1 and P_2O_2 make with H_1H_2 using Eq. (5) as follows:

$$\beta_i = \tan^{-1}\left(\frac{\sqrt{d^2 - \delta_i^2}}{\delta_i}\right), \quad i = 1, 2, \qquad (9)$$
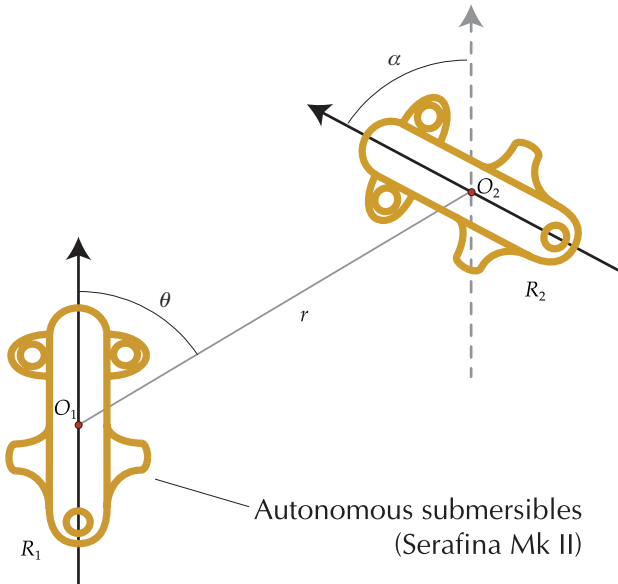
Figure 12. Azimuth θ, range r, and heading α of sending AUV R_2 with respect to the observing AUV R_1.
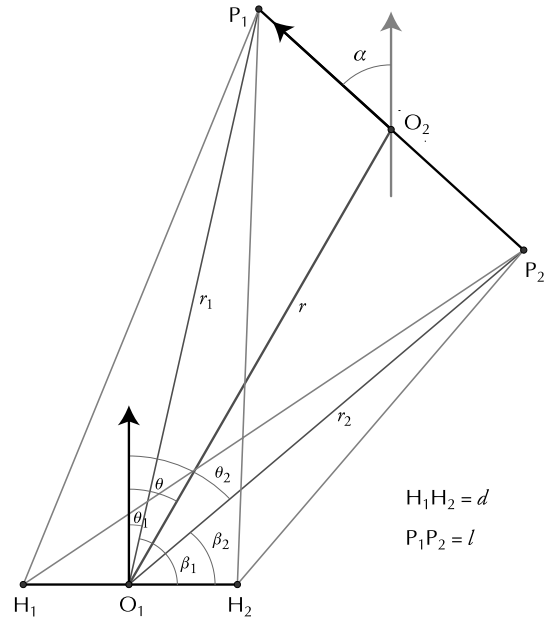
Figure 13. The geometric description of the angles and distances used to calculate the components of the pose vector, azimuth θ, range r, and heading α. Here θ_1 and θ_2 are subazimuths and r_1 and r_2 are subranges.

where d is the base distance between the hydrophones H_1 and H_2. δ_1 and δ_2 are the acoustic path length differences calculated according to Eq. (7), based on the two TDOAs corresponding to the two MLS signals emitted from P_1 and P_2. The two angles returned by Eq. (9) need to be transformed to θ_1 and θ_2 using

$$\theta_i = [90 \deg - \beta_i]_{\text{adj}}, \quad i = 1, 2, \qquad (10)$$

where the adjustment function $[\cdot]_{\text{adj}}$ is defined as

$$[x]_{\text{adj}}$$
$$= \begin{cases} x, & -180 \deg < x \leq 180 \deg \\ \text{sgn}(x)(|x| - 360 \deg), & x \leq -180 \deg, x > 180 \deg \end{cases}, \qquad (11)$$

which return the angles conforming to the measuring convention.

This adjustment is required because Eq. (5) produces β_i with the range -180 deg $< \beta_i \leq 180$ deg when implemented with the $\tan^{-1}(x, y)$ function, which considers the quadrant of the complex value $x + iy$, where $y/x = \tan \beta$. However, in the experimental implementation of the relative localization system, the range of Eq. (5) was limited to 0 deg $\leq \beta_i \leq 80$ deg due to the directivity of the hydrophones used. The two angles θ_1 and θ_2 give the azimuth estimate as

$$\theta = (\theta_1 + \theta_2)/2. \qquad (12)$$

Journal of Field Robotics DOI 10.1002/rob

4.2. Distance Estimation

The TOF of a signal is usually used to estimate the distance between the signal source and the receiver. The direct-path range estimation using the TOF of acoustic signals employed in this work is related to the spherical positioning schemes used in acoustic beacon–based underwater localization (Olson, Leonard, & Teller, 2006).

To measure the travel time of a signal, knowledge of the exact time at which the signal was emitted is required. This is achieved by maintaining explicitly synchronized clocks at both the receiver and transmitter locations when localizing relative to acoustic beacons. The logical time-step concept used in the relative localization system achieves synchronization in an implicit manner compared to maintaining clocks synchronized with absolute time. The long-wave radio communication system onboard each Serafina Mk II AUV, which transmits according to a distributed omnicast routing schedule (Schill & Zimmer, 2006, 2007), is coupled to the relative localization system such that each acoustic sending event is initiated simultaneously with the start of a long-wave radio transmission from a sender AUV, which also marks the start of a logical time step. Upon receiving the long-wave radio signal, each of the observer AUVs within communication range increments its respective logical clocks, marking the start of their logical time steps.

Owing to the significant difference in speed of propagation for electromagnetic and acoustic signals underwater, it can be safely assumed that the long-wave radio signal reaches an observer AUV earlier than the acoustic signal. The consequent start of the logical time step on the observer triggers the acoustic receivers, which begin to await the acoustic signal. If it takes time t for the acoustic signal to arrive since the start of the logical time step, the distance between the sender and the observer is

$$r = (t v_e v)/(v_e - v), \qquad (13)$$

where v_e and v are the speeds of propagation for electromagnetic and acoustic signals in water. However, with the relatively short distances between AUVs in a local neighborhood and comparing the magnitudes of the quantities[10] v_e and v, it can be assumed that the long-wave radio signals are transmitted between the neighboring vehicles instantaneously, which reduces Eq. (13) to

$$r = tv, \qquad (14)$$

where t can be expressed as the TOF of the acoustic signal.

4.2.1. Modified Matched Filter for TOF Extraction

In one of the early contributions to echo signal detection, Turin (1960) introduced the concept of matched filter pro-

cessing as a means for recovering a known waveform from a noisy signal. In its conventional form, a noise-free replica of the original signal is cross correlated with the received signal channel to locate the return signal and thus extract the TOF. In their work, Hermand & Roderick (1993) introduced an improved "model-based" matched filter that uses a copy of the original signal that is convolved with the impulse response of the transmission medium as the reference signal instead of a noise-free replica. This approach requires some a priori knowledge about the characteristics of the underwater environment in which the AUVs operate in order to construct the impulse response.

The proposed relative localization system uses an actual received signal channel as the reference for cross correlation. The system initializes with a prerecorded reference channel consisting of the MLS signal (which is used by the localization system as the source signal waveform) that has been transmitted and received underwater via the transducers used in the system.

The cross-correlation scheme described in the preceding section is used for this "modified" match filter as well, where one signal channel is replaced by the reference signal in work presented by Bellingham, Consi, Tedrow, and Di (1992). Two cross correlations are performed to extract the TOF to each of the two receivers for each signal received from the sender AUV. The diagram given in Figure 14 shows the four TOFs associated with the two pings. TOFs t_{11} and t_{12} are related to the front (bow) ping, and TOFs t_{21} and t_{22} are related to the rear (stern) ping. The long-wave radio signal emitted from the sender simultaneously with the first acoustic ping is assumed to be received instantaneously by the observer, triggering the start of the sending event. The subsequent TOFs are measured from this starting trigger. When implemented in hardware, there is finite latency and timing jitter associated with detection of the long-wave signal and the synchronized sending of the acoustic pings. If this synchronization latency of the receiving hardware is denoted by t_L, then the sample-domain
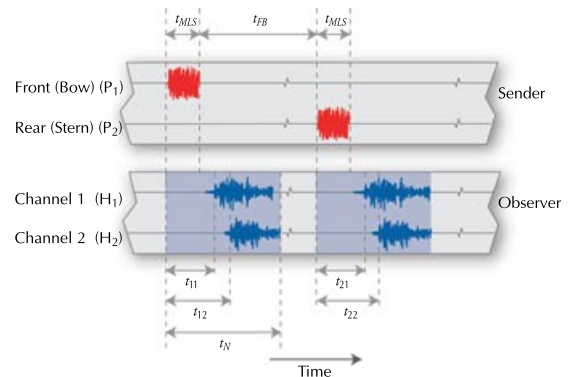
Figure 14. Time durations involving the sender and observer within one sending event.

---

latency τ_L is $f_s t_L$, where f_s is the sampling rate. The variation in latency, which is defined as timing jitter, is denoted by Δt_L. Its sample domain counterpart is

$$\Delta \tau_L = f_s \Delta t_L. \tag{15}$$

Without loss of generality, the range estimation will be explained in the next section using only the two TOFs where the bow (front) ping is the source signal. For this purpose, the two sample-domain delays obtained from Eq. (7) corresponding to the receivers H_1, H_2 are denoted by τ_0^{11} and τ_0^{12} with regard to a signal transmitted from P_1 (Figure 10) and the two TOFs t_{11} and t_{12} can be calculated as

$$\begin{aligned} t_{11} &= \left(\tau_0^{11} - \tau_L\right)/f_s, \\ t_{12} &= \left(\tau_0^{12} - \tau_L\right)/f_s, \end{aligned} \tag{16}$$

where τ_L is the sample-domain latency given in Eq. (15) and f_s is the sampling frequency of the analog-to-digital converters used.

4.2.2. Distance Estimation Using TOF

In spherical localization, measuring the travel time of an acoustic signal emitted by a single synchronized beacon with a known location defines a sphere centered at the beacon on which the receiver must lie (Deffenbaugh et al., 1996). Conversely, if the position of the beacon is unknown, the signal source must lie on a sphere centered at the receiver. In the planar case considered in the relative localization system, the said sphere reduces to a circle. However, instead of the multiple spheres (or circles in the planar case) needed to uniquely identify a position as done in traditional spherical localization, using a single circle and its intersection with the line defining the angle of arrival of the signal, which was described in the preceding sections, uniquely defines the position of the signal source.

To achieve better accuracy, two circles centered at the two receivers at H_1 and H_2 and the line defining the angle of arrival are used as shown in Figure 10. The radii of the circles centered at H_1 and H_2 denoted by r_{11} (=P_1H_1) and r_{12} (=P_1H_2) are obtained by substituting Eq. (16) in Eq. (14). The distance r_1 (=P_1O_1) needed to complete the polar coordinates (r_1, β) of signal source P_1 can be derived by

$$r_1 = \sqrt{\frac{r_{11}^2 + r_{12}^2}{2} - \left(\frac{d}{2}\right)^2}, \tag{17}$$

where d (=$H_1 H_2$) is the spacing between the receivers. In practice the distance between the hydrophones will always be at least one order of magnitude smaller than the distance between the vehicles.

As with the azimuth, instead of a single range measurement, the actual measurements are the distances to the sound sources P_1 and P_2 from each of the receivers H_1 and H_2. If P_1H_1, P_1H_2 are denoted as r_{11}, r_{12} and P_2H_1, P_2H_2 as

r_{21}, r_{22}, the distances r_1 (P_1O_1) and r_2 (P_2O_1) can be calculated using Eq. (17) as follows:

$$r_i = \sqrt{\frac{r_{i1}^2 + r_{i2}^2}{2} - \left(\frac{d}{2}\right)^2}, \quad i = 1, 2, \tag{18}$$

where d is the distance between hydrophones on the observer vehicle. Once r_1 and r_2 are calculated, the range r can be calculated using the formula

$$r = \sqrt{\frac{r_1^2 + r_2^2}{2} - \left(\frac{l}{2}\right)^2}, \tag{19}$$

where l is the separation between the projectors on the sender vehicle.

4.3. Heading Estimation

The heading α is the relative rotation angle between the polar axes of R_1 and R_2, measured with respect to the observer, R_1. As depicted in Figure 12, it can be seen as translating the coordinate system of R_1 onto R_2, such that the two poles coincide, and then measuring the angle between the two polar axes. That is, for whatever azimuth, if the two AUVs are traveling (or pointing) in the same direction (same heading), then the relative heading of R_2 measured by R_1 would be 0 deg.

The relative heading α of the sender vehicle as seen by the observer vehicle can be estimated with the aid of the component measurements θ_1, θ_2, r_1, and r_2 used earlier to derive the azimuth and the range. The range-adjusted heading can be expressed as

$$\alpha = \left[\tan^{-1}\left(\frac{r_1 \sin\theta_1 - r_2 \sin\theta_2}{r_1 \cos\theta_1 - r_2 \cos\theta_2}\right)\right]_{\text{adj}}, \tag{20}$$

where the θ_i values are given by Eq. (10) and the r_i values are given by Eq. (14). The adjustment function is the same as given in Eq. (11). Whereas $r_1, r_2 \geq 0$, by inspecting Figure 13 it is also clear that they cannot both be zero at the same time given the constraint $l > d$, which holds true in practice.

4.4. Reverse Hyperbolic Localization

The azimuth estimation presented in the preceding sections is based on hyperbolic localization (TDOA measurement) schemes, whereas the range estimation is based on spherical localization (TOF measurement) schemes. Overall, the source localization presented can be viewed as a hybrid approach. The heading estimation relies on the azimuth and range as shown by Eq. (20). However, the range estimation and the subsequent heading estimation require implicit synchronization between the sender and observer as with traditional TOF-based spherical localization schemes. This synchronization provided by the underlying communication scheduling system enables the relative localization system to measure TOF as described in Section 4.2.

With the two sound sources at P_1, P_2 and the two receivers at H_1, H_2, a novel reverse hyperbolic scheme was devised to calculate the range and heading that does not require a TOF measurement, consequently eliminating the dependence on sender–observer synchronization.

4.4.1. Reverse Azimuth Estimation

The acoustic path length differences δ_1 ($P_1H_1 - P_1H_2$) and δ_2 ($P_2H_1 - P_2H_2$) mentioned earlier were based on the two hyperbolas centered on H_1 and H_2 corresponding to the two acoustic sources at P_1 and P_2. By considering two more path length differences denoted by η_1 and η_2, which are equivalent to the quantities $P_1H_1 - P_2H_1$ and $P_1H_2 - P_2H_2$, two additional hyperbolas centered on P_1 and P_2 can be realized. The diagram in Figure 15 depicts the two hyperbolas centered on H_1, H_2 in blue (dashed) and the two hyperbolas centered on P_1, P_2 in red (dotted).

The observer vehicle receives four acoustic signal channels for each sending event. They comprise two channels received by the hydrophones H_1, H_2 with P_1 as the source, denoted by $x_{11}(t)$, $x_{12}(t)$, and the two channels received with P_2 as the source, denoted by $x_{21}(t)$, $x_{22}(t)$. The values for δ_1 and δ_2 were obtained from Eq. (8) after performing cross correlation as described in Section 4.1 on the channel pairs $x_{11}(t)$, $x_{12}(t)$ and $x_{21}(t)$, $x_{22}(t)$, respectively. Similarly, cross-correlating channel pairs $x_{11}(t)$, $x_{21}(t)$ and $x_{12}(t)$, $x_{22}(t)$ would give the corresponding sample-domain delays, which can be converted to the required path length differences η_1 and η_2 as $\eta_i = \acute{\tau}_0^i v/f_s$ with $i = 1, 2$ and where v is the speed of sound in water and f_s the sampling frequency of the analog-to-digital converter. $\acute{\tau}_0^1$, $\acute{\tau}_0^2$ are the sample-domain delays that maximize the respective cross-correlation functions. Just as β_1 and β_2 defined the angles P_1O_1 and P_2O_1 made with H_1H_2, two new angles φ_1 and φ_2 can be defined as the angles H_1O_2 and H_2O_2 make with P_1P_2. These two angles can be obtained from a slightly
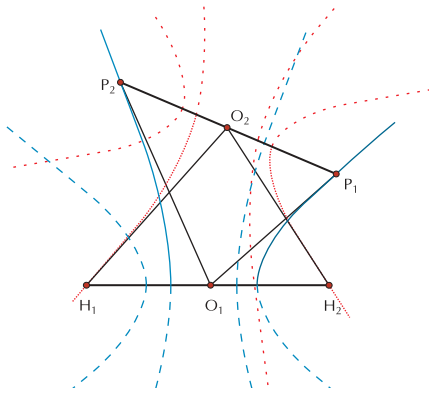
Figure 15. The two hyperbolas centered on P_1, P_2 depicted in red (dotted) and the hyperbolas centered on H_1, H_2 shown in blue (dashed).
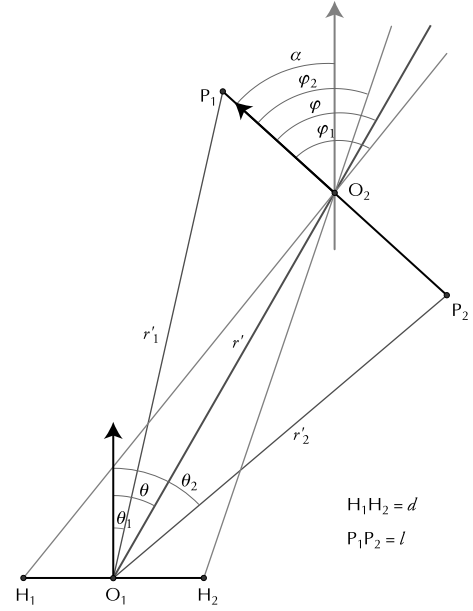
Figure 16. The geometric description of the new angles φ_1, φ_2 and φ their relationship to azimuth θ and alternate values for range $\acute{r}$ and heading $\acute{\alpha}$.

modified version of Eq. (14) using the path length differences η_1 and η_2 as follows:

$$\varphi_i = \text{sgn}^*(\theta_2 - \theta_1) \tan^{-1}\left(\frac{\sqrt{l^2 - \eta_i^2}}{\eta_i}\right), \quad i = 1, 2, \quad (21)$$

where l is the separation between the two projectors P_1, P_2 and the modified sign function is defined as

$$\text{sgn}^*(y) = \begin{cases} y/|y|, & |y| > 0 \\ 1, & y = 0 \end{cases}. \quad (22)$$

The angles returned from Eq. (21) have the range -180 deg $< \varphi_1, \varphi_2 \leq 180$ deg and give the reverse azimuth angle as $\varphi = (\varphi_1 + \varphi_2)/2$. The geometry of these quantities along with the measuring convention is shown in Figure 16.

4.4.2. Heading and Range Estimates Based on Reverse Azimuth

According to the geometry shown in Figure 16, an alternate relative heading $\acute{\alpha}$ of the sender with respect to the observer vehicle can be given as

$$\acute{\alpha} = [\varphi - \theta]_{\text{adj}}. \quad (23)$$

The adjustment function is the same as given in Eq. (17). The azimuth θ is as given by Eq. (12). A new calculation for range based on the reverse azimuth φ and $\acute{\alpha}$ derived above
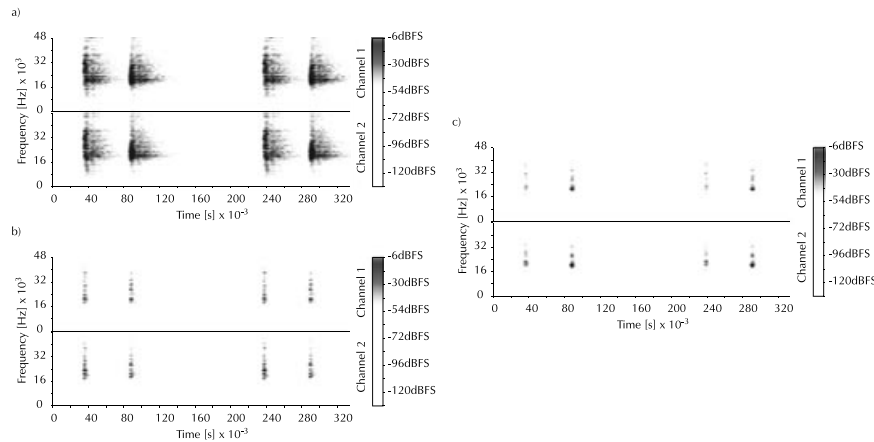
Figure 17. Spectrogram showing received hydrophone channels corresponding to two consecutive sending events (a) during an experiment in the test tank with $r \approx 2$ m and (b) and (c) during two experiment in the lake with $r \approx 8$ and 20 m, respectively.

yields $\acute{r}$ as follows:

$$\acute{r} = \left| \frac{d \cos(\varphi_1 + \acute{\alpha})}{2 \sin[\theta - (\varphi_1 + \acute{\alpha})]} \right|, \quad (24)$$

where d is the base distance between the hydrophones H_1, H_2. The other variables have the ranges $-180 \deg < \varphi_1$, $\acute{\alpha}, \theta \le 180 \deg$. As explained in Section 4.3, even though Eq. (24) allows for $\acute{r}$ to be zero, in practice it is always strictly greater than zero.

As these alternate calculations are based on two hyperbolas, each with foci at P_1 and P_2, considering their asymptotes that pass through H_1 and H_2, substituting these points in the polar coordinate equations for O_2H_1 and O_2H_2 and adjusting for the measuring conventions, the separate range components can be calculated using the following formula:

$$\acute{r}_i = \left| \acute{r} \cos(\theta_1 - \theta) \pm \text{sgn}^*(\acute{\alpha})\text{sgn}^*(\theta) \right.$$
$$\left. \sqrt{\left| \acute{r}^2 \cos(\theta_1 - \theta)^2 - \left[\acute{r}^2 - \left(\frac{l}{2} \right)^2 \right] \right|} \right|, \quad (25)$$

where the $+$ sign yields $\acute{r}_1$ and the $-$ sign yields $\acute{r}_2$. The variables have the following ranges; $\acute{r}, l > 0$, $-180 \deg < \theta_1$, $\acute{\alpha}, \theta \le 180 \deg$, and the modified sign function is as defined in Eq. (22). The sign functions are used in this formula to resolve the ambiguity introduced by the existence of two asymptotes per hyperbola mentioned earlier.

4.5. Handling Interference

Interference experienced by the acoustic signals used in the relative localization system can be broadly classified into three categories.[11] The first category is interference of the

direct-path signals by reflected (multipath) signals when operating in highly cluttered, reverberant environments. The second category, which has a similar effect on the localization system, is the interference in the presence of multiple sending events within a two-hop neighborhood due to colliding sending schedules. The underlying scheduling scheme, depending on the routing algorithm used, can produce colliding sending events within a local neighborhood. The third category of interference occurs due to extraneous acoustic sources present in the environment. Whereas detrimental effects due to this form of interference are largely avoided by the use of MLS signals, in the presence of intense broadband noise, the SNR can deteriorate to a level at which the TDOA measurement could yield estimates that correspond to the angular position of the noise source rather than the signal source. Furthermore, deterioration of the SNR can occur in two ways, with either higher noise levels or lower signal levels (as the signal source reaches the sensing limits of the receivers).

4.5.1. Cluttered Environments and Multiple Senders

Operating in cluttered, reverberant environments, the acoustic source localization is susceptible to inaccurate position fixes due to multipath arrivals of the signal. The test tank[12] in which the relative localization system was experimentally evaluated constitutes such a harsh acoustic environment with strong reverberations. Figure 17(a) shows a spectrogram[13] of the two received hydrophone channels corresponding to two consecutive sending events (each consisting of two MLS pings) recorded during an experiment in the test tank. The broadband intensity of the

---

[11]Some texts refer to these effects as reverberation, cross talk, and noise.

[12]Cylindrical tank with corrugated metal walls filled with tap water. Diameter 4.2 m, depth 1.5 m.

[13]Generated with short-time Fourier transforms with a window size of 512 samples.

reflected signals decays slowly, with frequencies near the resonance of the transducers ($\sim 20\,\text{kHz}$) being the most persistent. Figures 17(b) and 17(c) show spectrograms of received channels recorded during two experiments conducted at lake Burley Griffin.[14] The difference in the intensity and persistence of reverberations within the two acoustic environments can be observed by comparing these spectrograms with the one shown in Figure 17(a). As a result of the delayed multipath signal arrivals, the cross correlations used by the relative localization system to measure TDOAs and TOFs would yield multiple peaks in close proximity to the peak representing the direct-path signal.

4.5.2. Propagation Loss, Causality, and Channel Windowing

In the case of long-wave radio signals used by the communication system, when multiple nearby sources simultaneously transmit, due to the high speed of propagation, the signals would arrive simultaneously at a receiver within range, regardless of the relative distances between each transmitter and the receiver. However, due to propagation loss through the media, the signal from the transmitter closest to the receiver appears stronger. This phenomenon was experimentally validated by Schill and Zimmer (2006) and shows that the communication system can indeed receive and decode messages sent from the nearer transmitter despite the theoretical network model suggesting otherwise. According to the results of experiments conducted with two long-wave radio transmitters and one receiver, it was found that collisions in which the signals could not be received occurred only in a relatively narrow band (less than 0.5 m on average) when the transmitters were approximately equidistant to the receiver. Owing to this, the communication system adopts a geometrical collision model in which a signal from the nearer source would be decoded and interpreted, under the assumption that the signal strength monotonically decreases with distance.

Although the above assumption does not hold true for long-range underwater acoustic channels (Urick, 1983), it is valid for the shorter ranges applicable to the intervehicle distances in a local neighborhood being discussed here. In addition to the higher received signal strength, when multiple sources send simultaneously,[15] the direct-path acoustic signals from a nearer source would also arrive *earlier* at the observer. This is due to the relatively slower speed of propagation of acoustic signals compared to the electromagnetic counterpart. This is very similar to the earlier scenario in which the direct-path signal is accompanied by delayed multipath signals when operating in reverberant environments. In both cases, the direct-path signal/signal from the nearer sender arrives first at the observer and yields a higher peak in the subsequent cross correlations due to the higher signal strength. However, if the simultaneous senders are approximately equidistant from the observer or if the multipath arrivals are caused by reflectors in very close proximity to the source, the resulting cross-correlation peaks would have very small temporal separation and will have similar peak heights, which in turn would cause errors in the final localization estimates. Considering the dynamic nature of mobile platforms operating in real environments, the effect of such situations on the localization estimates is assumed to be transient. The peak tracking scheme introduced in Section 4.6.1 attempts to address such effects.

As mentioned in Section 3.2.1, the maximum effective range of the relative localization system is enforced by applying a truncating window upon the received signals. This scheme is similar to the *precedence effect* phenomenon studied in human hearing and binaural localization research and truncates the two hydrophone channels in the time domain. Owing to the synchrony introduced by the omnicast routing scheme, sending events throughout the swarm are triggered simultaneously. Therefore, acoustic pings from distant senders (beyond the one-hop neighborhood of an observer) during a particular sending event will arrive much later than the ping from a local sender (within the one-hop neighborhood of an observer). The aforementioned windowing scheme prevents acoustic signals from far (nonlocal) senders from affecting the subsequent cross correlations.

In the test tank experiments presented in Section 5, the delayed multipath signals act as interfering pings emitted simultaneously from distant sources. The windowing technique mentioned earlier and implemented in these experiments was effective in discarding most of these interfering signals. The interfering events not handled in this manner (reflected signals that are within the sensing range) are handled via the peak tracking scheme.

4.5.3. Experimental Evaluation of Cross-Talk and Reverberation Handling

The performance of peak detection by the relative localization system was experimentally tested in a situation in which the detrimental effects of a reverberant environment and multiple colliding sending events were combined.

First, two identical 128-sample MLS pings were emitted simultaneously from two projectors placed approximately equidistant[16] from the observer (hydrophone pair) to emulate two senders within its one-hop neighborhood.

---

[14]Lake Burley Griffin has an approximate surface area of 6.64 km^2 and is situated in the center of Canberra, ACT, Australia.

[15]Based on the assumption that the logical clocks are in sync up to sufficient accuracy (Schill, 2007, pp. 111–112).

[16]2.05 and 2.30 m from the observer, which induces an offset of 0.25 m. This is well within the "collision" band of approximately 0.50 m experienced by the long-wave radio communication system during experiments presented by Schill and Zimmer (2006).
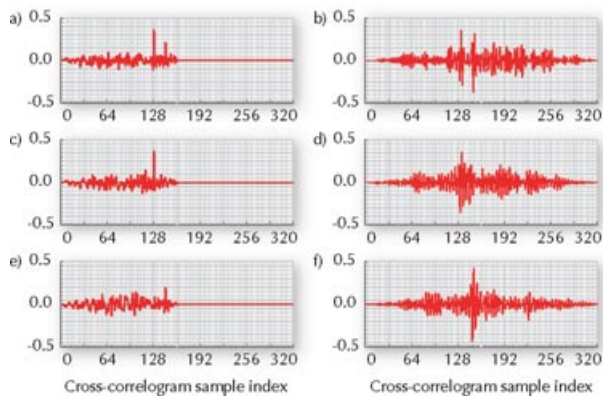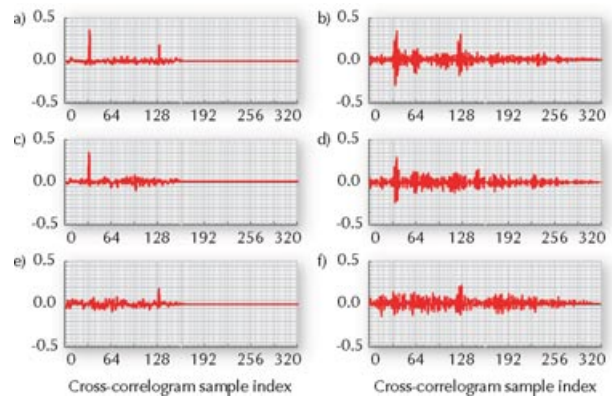
Figure 18. Cross correlograms from "simulated" uncorrupted MLS signals (left) and experimentally recorded signals (right). Two identical MLS signals (first row) and two different MLS signals (second and third rows) were used as sources. The two projectors were offset by 0.25 m.

Figure 19. Cross correlograms from "simulated" uncorrupted MLS signals (left) and experimentally recorded signals (right). Two identical MLS signals (first row) and two different MLS signals (second and third rows) were used as sources. The two projectors were offset by 1.40 m.

The duration of the pings was approximately 1.3 ms due to the sampling rate of 96 kHz. The received channels contained the two direct-path arrivals of the pings overlapping each other by more than 85% due to the placement and simultaneous emission in addition to the multiple delayed arrivals due to reflections. Figure 18(b) shows a cross correlogram used to extract the TOF for subsequent range estimation by the relative localization system using the modified matched filter introduced in Section 5.2. For comparison, Figure 18(a) shows a cross correlogram obtained by applying the matched filter to two identical uncorrupted MLS signal channels (as opposed to the experimentally recorded signal channels) of 1.3-ms duration, which were mixed such that they overlap each other by 87.5%.

Later, two different MLS signals were emitted from the same projectors without changing their positions. The modified matched filter was applied to the received hydrophone channels twice, corresponding to the two different MLS source signals. Figures 18(d) and 18(f) show two cross correlograms resulting from this process, each showing a peak region corresponding to one of the source signals. The corresponding cross correlograms obtained by the matched filter with uncorrupted MLS signals are shown in Figures 18(c) and 18(e) for comparison.

The same experimental procedure was repeated with the two projectors placed 0.55 and 1.95 m away from the hydrophone pair. First, two identical MLS pings were emitted simultaneously as before. Owing to this spatial configuration, the received channels contained the two direct-path arrivals of the pings overlapping each other by 30%. One of the cross correlograms resulting from the modified matched filter is shown in Figure 19(b). Later, two different MLS pings were emitted simultaneously from the two projectors, and two cross correlograms resulting from the corresponding matched filter processing are shown in

Figures 19(d) and 19(f). As before, corresponding cross correlograms resulting from applying the matched filter to uncorrupted versions of the MLS signals are shown in Figures 19(a), 19(c), and 19(e) for comparison.

Cross-correlogram peak regions of the experimentally recorded signals presented earlier show the impact of spatial separation of the sending events in the absence of temporal separation. All cross correlograms resulting from matched filter processing of experimentally recorded hydrophone channels also show the effect of multipath arrivals due to reflections. Secondary peak regions in these cross correlograms have relatively lower heights compared to the primary peak regions caused by the two direct-path signals. This can be attributed to the lower signal strengths of the reflected signals. In the second instance, in which the relative spatial separation between the projectors was increased to 1.4 m from the earlier 0.25 m, the primary peak region from the far source has a lower height than the primary peak region from the near source. Here, one of the prominent secondary peak regions due to a strong reflection of the near source (off the bottom of the tank, 0.5 m below the near source) still has a lower peak height compared to the primary peak region of the far source. Therefore, as long as there is minimal relative spatial separation (down to 0.25 m as presented in the earlier experiments), the relative localization system can resolve acoustic signals emitted from simultaneous sending events initiated within the one-hop neighborhood of an observer. In the case of reverberant environments, assuming that direct-path signals have a higher signal strength[17] than the delayed

---

[17]This assumption holds true except in situations in which reflected signals can appear louder than the direct-path signal due to the nonomnidirectional directivity pattern of the receivers used.

multipath arrivals, the relative localization system can still accurately resolve the acoustic source position. The precision of the localization estimates produced in reverberant environments is further improved by the peak tracking scheme introduced in Section 4.6.1, which deals with transient outliers.

4.5.4. Interference from Extraneous Noise Sources

For a given constant source signal strength, the SNR on the received channels could deteriorate in either of two ways: with a higher noise level or with lower signal levels induced by the source position reaching the sensing limits of the receivers. Effects of spurious noise are largely avoided by the use of MLS signals as the acoustic source. In the face of broadband noise, cross correlation of MLS signals were shown in Section 2.3 to withstand a SNR as low as 0 dB. The effect of lower SNR manifests itself in lowering the peak height in the ensuing cross correlations but does not directly contribute to alter the peak position. In the experimental results given in Section 5, it is shown that the relative localization system can produce accurate localization estimates under conditions in which the SNR is near 0 dB.

4.6. Handling Outliers

The general approach of position estimation schemes is to assume that the position of the target changes in time according to a dynamic model in response to some control input and noise. The sensor that observes the position of the target produces readings according to some measurement model that are also corrupted by noise. Under these circumstances, initial/previous position estimates and initial/previous error (noise) distributions are used to predict the time evolution of these quantities and to update them with the information gathered from the actual measurement in the current time step to produce a current position estimate. The effectiveness of the approaches is improved with additional knowledge about the motion characteristics of the localization target and more precise information about the measurement/noise models, as explained in detail by Bar-Shalom, Kirubarajan, and Li (2002). Extended Kalman filters (EKF) and particle filters (Gordon, Salmond, & Smith, 1993) are among the most popular approaches used for position estimation. Leonard and Durrant-Whyte (1991) present an EKF-based approach for localization and tracking of a mobile robot equipped with sonar sensors. More recently Olson, Leonard, and Teller (2004) present an EKF technique for outlier rejection in long-baseline (LBL) navigation for AUVs. Thrun, Fox, Burgard, and Dellaert (2001) present an improved particle filtering approach called mixed Monte Carlo localization while discussing the attributes and drawbacks of conventional methods.

   Instead of a particular sensor providing a noisy measurement (e.g., odometry, laser range finder, sonar sensor,

vision processing system), which is then used as the input to a localization system, the relative localization system presented in this article itself is treated as a "sensor" that produces a position estimate with the possibility of handling outliers at a very low level in the localization processing chain. Instead of rejecting outliers and estimating a position based on a posterior error distribution given a noisy measurement per time step, the raw data (cross correlograms used for TDOA and TOF measurements) of the relative localization system at each time step are seen as containing true position information along with many outliers caused by environmental interference. Therefore the emphasis is on recovering the true position rather than on rejecting the outliers. The view that the raw data contain the true position along with outliers is shared by Ward, Lehmann, and Williamson (2003) in their work regarding acoustical source localization in reverberant indoor environments. They assume that the true position will follow a dynamic model in time evolution and the outliers will show no temporal consistency between time steps. Empirical data collected while experimentally evaluating the relative localization system presented in this text suggest that only the first part of the assumption holds true. The outliers caused by side-lobe peaks in the cross correlograms, especially when operating in reverberant environments, follow a dynamic model very similar to the true position.

   While avoiding drawbacks of conventional approaches and drawing insights from Markov localization methods (Arulampalam, Ristic, Gordon, & Mansell, 2004), a novel yet simple strategy for peak recovery from the measurement cross correlograms is presented next. This peak tracking scheme uses a local maxima search to "predict" the true peak position and exploits the underlying subsample interpolation scheme to "update" and refine the peak position.

4.6.1. Peak Tracking

Whereas Eq. (7) in Section 4.1 suggests a simple routine for finding the peak of a cross correlogram and the corresponding position of the peak, the following peak tracking scheme contributes to effective handling of outliers arising due to interference. The main feature of this scheme is that it enforces continuity assumptions of the estimated quantities. Apart from the assumption that the variation of peak position in sample space follows a Markov process (i.e., current peak position depends only on the previous peak position) and a priori information about maximum variation of each raw estimate,[18] this method does not rely on specific motion models, sensor models, or error distributions. Furthermore, because the update and refinement of the peak

---

[18]Maximum physically possible sample space variation within one estimation step based on maximum angular and linear relative velocities between observers and senders.
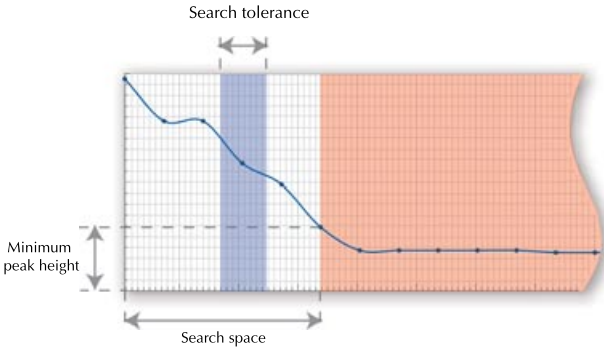
Figure 20. Local maxima search space and tolerance on a cross correlogram sorted by peak magnitude.

position are done with the underlying subsample interpolation scheme, the additional computational cost is minimal.

Here $R_{s_1 s_2}$ refers to the full-range cross correlation of two length-N signal channels $s_1(n)$ and $s_2(n)$, which include both positive and negative discrete lags in sample space. For clarity, the following sections will always refer to a cross correlogram spanning a sample space of $\{-N \ldots N\}$, but in the actual implementation, the cross correlations related to azimuth estimation and reverse azimuth estimation are limited to lags between $-f_s d/v$, $f_s d/v$ and between $-f_s l/v$, $f_s l/v$, respectively. The cross correlation corresponding to the matched filtering required for the direct range estimation spans the full $-N$ to N range.[19] An "element" of the resulting cross correlation with a lag of n samples can be expressed as $x(n) \in \{x_{-N} \ldots x_N\} = R_{s_1 s_2}$. $X(n)$ is defined as a set containing all ordered pairs of lags and corresponding values of the cross correlogram as $X(n) = \{(n, x(n)), \forall n \in \{-N \ldots N\}\}$. Another set $X_{\text{sorted}}(m)$ is formed by sorting $X(n)$ in descending order by the value of $x(n)$ as $X_{\text{sorted}}(m) = \{(m, y(m)), \forall m \in \{-N \ldots N\}\}$, where $n, m \in \{-N \ldots N\} \subseteq \mathbb{Z}$, $x(n), y(m) \in [-1, 1] \subseteq \mathbb{R}$. Whereas $X_{\text{sorted}}(m)$ and $X(n)$ are bijective, the following condition is also satisfied by the elements of $X_{\text{sorted}}(m)$:

$$\forall m \in \{-N \ldots (N-1)\}, \quad y(m) \geq y(m+1). \tag{26}$$

A set $M(k)$ corresponding to estimation step[20] k is defined as follows:

$$M(k) = \{m \in \{-N \ldots N\}\}, \quad \text{s.t. } |m - \tau_0^I(k-1)| < \Delta_{\text{Tolerance}}, \tag{27}$$

where m is drawn from the ordered pairs in the set $X_{\text{Sorted}}(m)$, $\Delta_{\text{Tolerance}}$ being a tolerance value based on the continuity assumptions of the quantity being estimated and

$\tau_0^I(k-1)$ being the subsample interpolated lag at estimation step $k-1$. The "refined" lag for estimation step k returned by the cubic spline interpolation function I_{Spline}, which takes in n_{Int} as a parameter, can be defined as

$$\tau_0^I = I_{\text{spline}}\left[\tau_0(k), n_{\text{Int}}\right]. \tag{28}$$

The lag of the new "tracked peak" of the cross correlogram that maintains continuity with the previous estimates denoted by $\tau_0(k)$ is the minimum element of $M(k)$ given as

$$\tau_0 = \min\{M(k)\}, \tag{29}$$

where $\tau_0(k) \in \{-N \ldots N\} \subseteq \mathbb{Z}$, $\tau_0^I(k) \in [-N, N] \subseteq \mathbb{R}$.

This procedure essentially performs a local maxima search of the cross correlogram within the neighborhood of lags around the previously estimated lag (Figure 20). Because elements of $M(k)$ are drawn from $X_{\text{Sorted}}(m)$, this guarantees that the lag returned by Eq. (29) corresponds to the highest peak within the search neighborhood. This discrete lag returned by Eq. (29) is then refined further by subsample interpolation using Eq. (28). The size of the search neighborhood is decided by the value selected for $\Delta_{\text{Tolerance}}$.

The lower bound for $\Delta_{\text{Tolerance}}$ is greater than or equal to the maximum possible lag in the sample domain corresponding to the variation of angles and distances within the duration between two estimation steps (one schedule slot) based on the relative angular and linear velocities between the observer and the sender. This can be expressed as $\Delta_{\text{Tolerance}} \geq |\omega_{\max}| f_s t_{\text{TS}}/v$, where t_{TS} is the duration of a schedule slot, f_s is the sampling frequency, v is the speed of sound in water, and $\omega_{\max}$ is a placeholder for maximum relative velocity between the observer and the sender.[21] The underlying assumption is that the position variations maintain continuity between estimation steps within the tolerance bounds. Because $\Delta_{\text{Tolerance}}$ is defined for one schedule slot and the localization system operates at minimum granularity of t_{TS}, irregular update rates in localizing a particular sender can be accommodated by modifying Eq. (27) as follows:

$$M(k) = \{m \in \{-N \ldots N\}\}, \quad \text{s.t. } |m - \tau_0^I(k-1)| < j\Delta_{\text{Tolerance}}, \tag{30}$$

where j is the number of schedule slots (multiples of T_{TS}) since the particular sender was previously localized. For the experiments presented in Section 5 that involved only one sender, this value remains at $j = 1$.

The motivation behind the implementation described above, which involves sorting the elements of the cross correlogram, was to provide a facility to dynamically limit

---

[19]Or $-N_{\text{RT}}$ to N_{RT} if range tracking is implemented as explained in Section 4.6.3.

[20]This also corresponds to the kth sending event initiated by the particular sender that is being localized.

[21]See Kottege (2009, pp. 235–236) for the derivation of lower bounds of $\Delta_{\text{Tolerance}}$ for maximum angular and linear relative velocities.

the search domain for lags to some $N_{\text{Restricted}} \leq N$ by restricting minimum $y(m)$ to some $y_{\min}$ in Eq. (27) [which in turn violates the bijectivity condition between $X(n)$ and $X_{\text{Sorted}}(m)$]. This condition is stated as $\forall (m, y(m)) \in X_{\text{Sorted}}(m), y(m) \geq y_{\min}$. This would specify a lower bound to the peak magnitude in the cross correlogram that can correspond to the lag returned by Eq. (29). As a consequence of the violation of the bijectivity condition, there could be situations in which $M(k) = \{\}$.[22] Therefore Eq. (29) needs to be reformulated as

$$\tau_0(k) = \begin{cases} \min\{M(k)\}, & M(k) \neq \{\} \\ \tau_0^*, & M(k) = \{\} \end{cases}. \qquad (31)$$

The value for τ_0^* can be either a constant position model or a constant velocity model by returning the previous lag $\tau_0^I(k-1)$ or $\tau_0^I(k-1)(1 + \nabla \tau_0^I(k-1))$, where $\nabla \tau_0^I(k-1)$ is the sample domain gradient of lags at the previous estimation step. Although this choice depends on the application, for the experimental evaluation of the system presented, the constant velocity model was used.

The parameter $y_{\min}$ can be used to control the behavior of the peak tracking system in the face of low received signal levels. As discussed earlier, for MLS signals, the peak height of cross correlograms is reduced as the SNR deteriorates. By having empirical knowledge of the peak heights caused by cross correlation of background ambient noise in the absence of a source signal, the relative localization system can be prevented from erroneously tracking noise sources as the signal source moves beyond the maximum sensing range of the receivers. This methodology was implicitly implemented for range estimation using the range tracking scheme introduced in Section 4.6.3.

There are multiple cross correlations per estimation step, which results in multiple sets for $M(k)$ used for estimating the intermediate quantities r_{11}, r_{12}, r_{21}, r_{22}, θ_1, θ_2, φ_1, and φ_2. For each of these quantities, there is a corresponding tolerance value $\Delta_{\text{Tolerance}}$ calculated using the maximum possible variation (constrained by the physical capabilities of the Serafina Mk II AUV/experimental setup) of the lags in the sample domain corresponding to variation of angles and distances within a schedule slot as mentioned earlier. As a "boot-strapping" technique, initially peak tracking is disabled and Eq. (7) is used to find the lags corresponding to the maximum magnitude peak in the cross correlogram as no prior estimate is available at initialization. Once the position of the peak stabilizes (e.g., detected by a result sequence that can be explained by the maximal relative speeds of the vehicles, i.e., no discontinuities over a certain number of estimation steps), peak tracking is enabled.

The success of this method greatly depends on the value chosen for the parameter $\Delta_{\text{Tolerance}}$. A lower bound for this parameter was defined in terms of maximum relative velocities between senders and observers; it is difficult to pick an optimal value without empirical measurements conducted in the operational environment to gauge the level of interference present. As $\Delta_{\text{Tolerance}}$ is increased, the ability of the system to recover true peak positions from nearby spurious outlier peaks would decrease. In this context, an upper bound for $\Delta_{\text{Tolerance}}$ can be specified as $\Delta_{\text{Tolerance}} \leq t_{\text{PT}} f_{\text{s}}$, where spurious peaks (higher than the peak due to the true position) due to multipath arrivals after t_{PT} seconds of the direct-path arrival are guaranteed to be handled by the peak tracking system. Multipath signals arriving before t_{PT} seconds have lapsed since the direct-path arrival (tolerance interval) do not affect the estimation system as long as the corresponding peak heights are lower than the peak due to the direct-path signal, which usually is the case.[23]

In the event of sustained occurrence of spurious peaks with higher peak amplitude than the true peak within the tolerance interval, the peak tracking scheme is susceptible to "latch on" and keep tracking the outlier peaks. In such a scenario, if the $\Delta_{\text{Tolerance}}$ value is selected too low, the tracking system could start wandering without being able to find the true peak. This would require a restart of the peak tracking system by reverting to a simple maxima search until the peak position stabilizes and then reenabling peak tracking. However, for an appropriately selected $\Delta_{\text{Tolerance}}$ value, the tracking scheme would recover within a few estimation steps and continue to track the "true" peak.[24]

4.6.2. Threshold Bounding

The primary estimates (azimuth, range, and alternative heading) are kept within bounds by restricting the extrema of lags produced by the relevant cross correlations. As mentioned in the preceding section, the cross-correlation lags for subazimuths and sub-reverse-azimuths are restricted in sample space between $-f_{\text{s}}d/v$, $f_{\text{s}}d/v$ and $-f_{\text{s}}l/v$, $f_{\text{s}}l/v$, respectively. Accordingly, this limits subazimuths and sub-reverse azimuths to $-90, 90$ deg and $0, 180$ deg, respectively, considering the extremes imposed by the physical dimensions that separate the hydrophones and projectors. The matched filter cross correlations for measuring subranges are limited to sample domain lags of $-N, N$ corresponding to the size of the channel window, which in turn reflects the maximum effective range of the localization system $r_{\max}$. This scheme guarantees that the localization system does not produce out-of-bound primary estimates.

---

[22]This could also be caused by a $\Delta_{\text{Tolerance}}$ value that is smaller than the lower bound stated earlier.

[23]Except in situations in which reflected signals can appear louder than the direct-path signal due to the nonomnidirectional directivity pattern of the receivers used.
[24]An example of self-recovery is discussed in Section 5.5.3.

The secondary estimates (heading and alternative range) that are calculated using the primary estimates can potentially produce out-of-bound values due to the numerical structure of the formulas used. However the adjustment function given by Eq. (17) ensures that heading estimates produced by Eq. (20) are always within bounds of -180, 180 deg. The outliers in alternate range estimation are handled by a combination of range checking and validation against gradients defined by maximum relative velocities. The threshold used for validating the alternate range estimate is $r_{\max}$ [because $\acute{r} > 0$ according to Eq. (24)]. For gradient validation a priori knowledge of the maximum possible linear relative velocities between the AUVs is used.

The procedure is as follows: if the position gradient induced by the current secondary estimate is greater than the gradient permitted by the maximum relative velocity, the estimate is replaced by either the previous estimate (constant position model) or an extrapolated value based on the gradient associated with the previous value (constant velocity model). As with the previously explained peak tracking scheme, the choice is dependent on the application. A constant velocity model was used in the range variation experiments presented in Section 5. The second validation involves a range check to see whether the secondary estimates (including those corrected by the gradient validation) are within the absolute threshold of $r_{\max}$ mentioned earlier. If the range check fails, the estimate is replaced by the threshold itself. If both gradient and range checks fail, the pose vector assembly module is meant to flag the estimate as invalid.

4.6.3. Range Tracking

The length of cross correlations used for direct range estimation scales up with increasing range and proves to be computationally costly for longer ranges. A range tracking scheme is proposed to overcome this problem. In this scheme, the truncated window of the received hydrophone channels is further cropped using information based on the time history of range estimates. The length of this secondary crop window N_{RT} is based on the maximum relative velocities of the submersible being localized and the time duration since the last localization of said submersible. The crop window is centered at r^i_{Previous}, which would be the estimated range of the sender (with node ID i) during the previous sending event initiated by the same sender. As discussed earlier, depending on the structure of the local communication schedule, a particular node may trigger multiple sending events within a given local schedule run. Apart from addressing the issue of high computational cost, the secondary crop window implicitly implements search space restriction in peak tracking related to range estimation. In this regard, the length of the secondary crop window N_{RT} is equivalent to $N_{\mathrm{Restricted}}$ mentioned in Section 4.6.1.

Table II. Values used for the peak tracking parameter $\Delta_{\mathrm{Tolerance}}$ during different experiments, of which results are analyzed in Section 5.4.
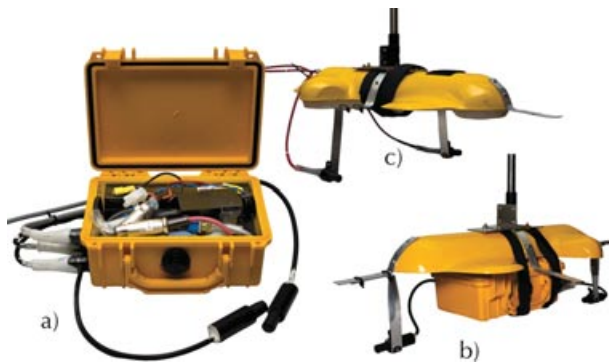
Experiment type	Variation	Value of $\Delta_{\mathrm{Tolerance}}$		
		For δ_1, δ_2	For η_1, η_2	For $r_{11}, r_{21}, r_{12}, r_{22}$
Tank	Azimuth	0.65	0.65	2.50
	Range	0.70	0.70	3.00
	Heading	0.62	0.62	1.00
Lake	Azimuth	1.00	1.50	3.50
	Range	1.00	1.50	2.50
	Heading	0.65	0.65	1.55
Long range	Combined	1.50	1.50	15.5

With range tracking enabled, once the start of a sending event is triggered, the sample counter on the observer resets and counts up to $r^i_{\mathrm{Previous}} f_{\mathrm{s}}/v - N_{\mathrm{RT}}/2$ and then starts assembling the first cropped channel window segment of length N_{RT}. The beginning of the second segment is aligned with sample number $r^i_{\mathrm{Previous}} f_{\mathrm{s}}/v - N_{\mathrm{RT}}/2 + t_{\mathrm{FB}} f_{\mathrm{s}} + l_{\mathrm{MLS}}$. As a consequence, the constraint on the maximum effective range given by relation (3) based on the delay t_{FB} no longer applies and defaults to the constraint given by Eq. (2), which is based on the duration of a scheduling time step t_{TS}.

This scheme greatly reduces the computational cost of the range estimation for longer ranges by transforming the computational complexity from $\mathcal{O}(N^2)$ to $\mathcal{O}(1)$ because the cross-correlation length N_{RT} no longer scales up with N due to increasing $r_{\max}$. However, this simple tracking scheme's effectiveness relies heavily on the accuracy of the previous range estimates. As a consequence, it is preferably used only when the local swarm configuration is stable with relatively slow changes in position. The effectiveness of this range tracking scheme was experimentally evaluated for long-range ($r > 10\,\mathrm{m}$) estimations, and the results are presented and analyzed in the following section.
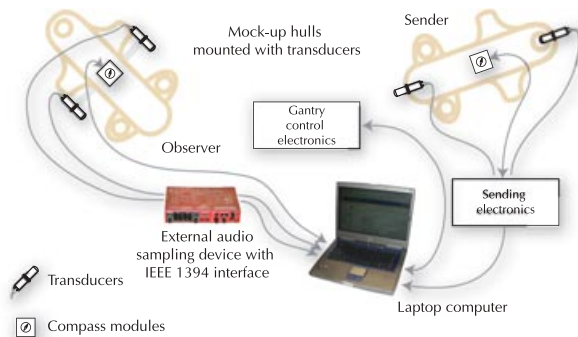
5. EXPERIMENTS

To evaluate the performance of the estimates produced using the formulations presented earlier, a number of experiments were carried out. Transducers were mounted on Serafina mock-up hulls to represent the sender and observer AUVs and were moved relative to each other in the Australian National University (ANU) test tank and at Lake Burley Griffin. Two mock-up hull rigs (observer and sender) fitted with hydrophones and projectors (Figure 21) and mounted at the end of shafts were moved relative to each other with the use of a robotic gantry placed on top of the test tank (for test tank experiments), mounted on the side of a pier (for lake experiments), or by attaching one rig
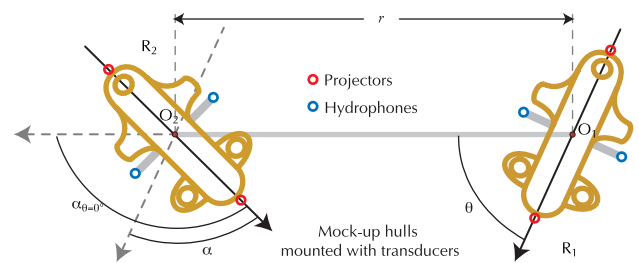
Figure 23. Possible variations in the experimental setup. The mock-up hulls with the transducers attached to the rigs can be rotated to vary the azimuth (θ) and heading (α), and the range (r) can be varied by moving the rigs along the rail on the gantry.

5.1. Experimental Procedure

A series of experiments were conducted to evaluate the performance of the relative localization system. Within the constraints of the directionality of the transducers used, experiments attempted to cover the full angular range for azimuth and heading estimates. This was achieved by rotating the shafts attached to the rigs by 180 deg using the gantry cart. The maximum distance measured at the tank was 2.25 m, with a translation of 1.5 m of the cart, and the maximum distance measured at the lake was 10.0 m with a translation of 2.0 m. The possible variations of the three parameters, azimuth (θ), heading (α), and range (r), using the experimental setup are shown in Figure 23. The long-range experiments in which the sender rig was attached to a kayak involved distances beyond 90 m. Table II gives the values used for the parameter $\Delta_{\text{Tolerance}}$ used during each of the experiments whose results are presented in this work.

5.2. Establishing Ground Truth

The heading readings of the two compass modules attached to the rigs and the linear position of the gantry cart were used to derive ground truth references for the estimated quantities. Whereas the linear positions were validated by actually measuring the initial and final positions of the gantry cart along the rail, the relative shifts of the compass heading readings were validated against the angular positions returned by the rotational motion servo motor on the gantry cart.

If r_s is the starting distance between the sender and the observer rigs for a particular experiment and the linear position returned by the gantry cart is r_g, then the ground truth for range is given by $r_0 = r_s - r_g$.

Because the compass readings are absolute heading angles relative to magnetic north, the relative angular positions were calculated by considering absolute headings from both the compass modules attached to the sender and the observer. If the absolute compass headings are denoted by α_{sender} and α_{observer}, then the relative variation of azimuth induced by a rotation of the observer defined

Figure 21. (a) Waterproof Pelican box housing the sending electronics to which the two projectors are connected, (b) sender rig with the Pelican box strapped to its belly and projectors fixed to the mounting points, and (c) observer rig with the two hydrophones fixed to the mounting points and the compass module strapped to its belly.

to a boat (for long-range lake experiments). The main relative localization system software was executed on a laptop computer running a standard non-real-time desktop operating system.

During the experiments, the base distance between hydrophones d was 0.3 m, the projector spacing l was 0.5 m, and the sampling frequency f_s used was 96 kHz. The speed of sound in water was calculated to be 1,497 ms^{-1}. An update rate of 5.0 Hz was used throughout the experiments. The signals received by the hydrophone pair were fed through to the computer from an external sampling device via the IEEE 1394 (firewire) bus. The sender–observer synchronization was provided by the sending electronics module signaling the start of sending events via the serial port (as a substitute for the radio communication synchronization signal, which was not available in the field experiments). Figure 22 illustrates the connectivity between these components.

Figure 22. The main components of the experimental setup showing data and control flows between them.

as the azimuth ground truth is given by $\theta_0 = [\alpha_{\text{observer}} - \alpha_{\text{sender}}]_{\text{adj}}$ and the relative variation of heading induced by a rotation of the sender defined as the heading ground truth is given by $\alpha_0 = [\alpha_{\text{sender}} - \alpha_{\text{observer}}]_{\text{adj}}$, where the adjustment function $[\cdot]_{\text{adj}}$ is defined as in Eq. (11) in both instances.

During the long-range experiments on the lake where one rig was mounted to a kayak, the derivation of ground truth for the relative position of the sender is different from the procedure explained above. All three parameters, azimuth, range, and heading, vary independent of each other through the course of these experiments. The azimuth and range ground truths were derived from the positions of the kayak recorded via the GPS module and data logger. For these experiments, at each time step, the ground truth for range is $r_0 = r_{\text{GPS}} - r_{\text{offset}}$, where r_{GPS} is the GPS distance returned by the data logger on the kayak and r_{offset} is the starting distance between the mounting points of the observer rig attached to the pier and the sender rig mounted to the kayak. The ground truth for azimuth is calculated using the longitude and latitude returned by the GPS data logger as follows:

$$\theta_0 = \tan^{-1}\left(\frac{x_{\text{sender}} - x_{\text{observer}}}{y_{\text{sender}} - y_{\text{observer}}}\right) - 90\deg + \theta_{\text{offset}}, \quad (32)$$

where x_{sender}, y_{sender} are the longitude, latitude coordinates returned by the GPS data logger on the kayak and x_{observer}, y_{observer} are the longitude, latitude coordinates of the mounting point of the observer rig. The θ_{offset} represents the correction for the relative rotation between the coordinate frame fixed on the observer hull and the longitude, latitude coordinate system (based on true north).

The deviations of pose vector components from their respective ground truth values are defined as estimation errors. Formulas are derived to analyze the statistical behavior of these deviations. In the following derivations, ϕ is used as a placeholder for θ, r, α, $\acute{r}$, and $\acute{\alpha}$. Therefore, the deviation of estimates with bias is given by $\Delta\phi_i^{\text{biased}} = \phi_i - \phi_0$, where ϕ_i is the estimate and ϕ_0 the corresponding ground truth at estimation step i. The mean $\mu_{\Delta\phi}$ of the estimation error for estimation steps is

$$\mu_{\Delta\phi} = \frac{1}{m}\sum_{i=1}^{m}(\phi_i - \phi_0), \quad (33)$$

and the standard deviation $\sigma_{\Delta\phi}$ of the estimation error for m estimation steps is

$$\sigma_{\Delta\phi} = \sqrt{\frac{1}{m}\sum_{i=1}^{m}\left(\Delta\phi_i^{\text{biased}} - \mu_{\Delta\phi}\right)^2}. \quad (34)$$

The unbiased root squared errors (RSE) of the estimate would then be given by

$$\Delta\phi_i = |\Delta\phi_i^{\text{biased}} - \mu_{\Delta\phi}|. \quad (35)$$

The average deviation of the RSE is given by

$$\Delta\phi = \frac{1}{m}\sum_{i=1}^{m}\Delta\phi_i, \quad (36)$$

where m is the number of estimation steps. Because there are no assumptions regarding the form of estimation error distribution, rather than the standard deviation given by Eq. (34), the average deviation given by Eq. (36) is considered to be a better indication of the behavior of the estimation error, being a more direct representation of empirical data.

5.3. Effects of Peak Tracking

An experimental run is used to analyze the effects of peak tracking on the different pose vector components when combined with inverse transducer response filtering. The first column of Figure 24 contains plots of δ_1, δ_2, η_1, and
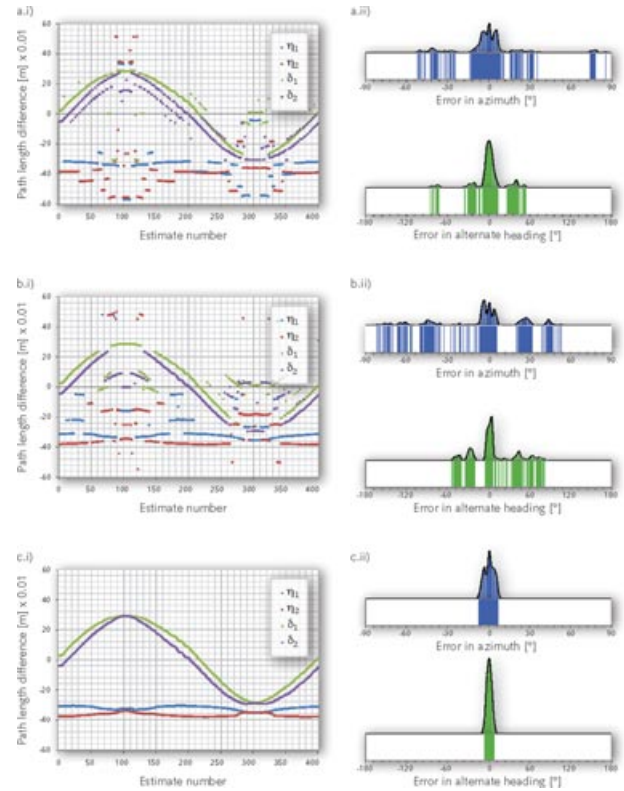
Figure 24. The intermediate values produced by the relative localization system that consists of the acoustic path length differences are plotted along with the errors of azimuth and alternate heading that are calculated using these values. The first row is with no filtering, and the second row is with inverse frequency response filtering applied to the hydrophone channels that are inputs to the cross correlation. The third row is with filtering applied and with peak tracking on the cross correlograms enabled.

η_2 produced during an experiment. In this experiment, the observer was rotated such that the azimuth ground truth varied as $\theta_0 : 0 \to -90 \to 0 \to 90 \to 0$ deg, while the sender was stationary with $\alpha_{\theta=0\,\text{deg}} = 100$ deg and $r_0 = 1.5$ m. Plot (a.i) was obtained using unfiltered hydrophone channels as the inputs to the cross correlation with no peak tracking on the cross correlograms, plot (b.i) was with the inverse frequency response filter applied but without any peak tracking, and plot (c.i) was with the filter applied and with peak tracking enabled. Plot (a.i) shows the effects of the adjacent side-lobe peaks that cause the outliers on either side of the main path length differences. The η_1 and η_2 estimates are more badly affected than the δ_1 and δ_2 estimates at this stage. When the filter is applied, a deterioration of the values around 100 and 300 estimates is clearly noticeable. These areas correspond to azimuths of -90 and 90 deg where the hydrophones on the observer are pointed in a direction almost perpendicular to projectors on the sender. Owing to the directivity pattern of the AQ-2000 hydrophones, which are nonomnidirectional, the direct-path signals that are received in these regions would carry most of their energy in frequencies within a narrow bandwidth centered at the resonance frequency of the transducers. The filtering process that aims to "smooth out" the received frequency spectrum by attenuating spikes caused by resonance contributes to further reduce the energy of the direct-path signals. Under these circumstances, the signals reflected off the curved metal walls of the test tank, which impinge on the hydrophones from the front, tend to carry more energy than the direct-path signals. Hence the cross-correlogram peaks due to reflections tend to have a higher amplitude than those due to direct-path signals in these regions, causing the performance of the estimation system to deteriorate when the filter is applied. However, peaks caused by direct-path signals occur *before* the peaks caused by reflected signals, albeit with much lower amplitude. The peak tracking algorithm exploits this fact and manages to retrieve the peaks caused by direct-path signals by considering peak positions in previous estimates. The results can be seen by comparing plots (b.i) and (c.i), where applying filtering and peak tracking (with $\Delta_{\text{Tolerance}} = 0.65$ for each of the four cross correlations) completely eliminates outliers in the path length difference measurements that are subsequently used for the angular estimations.

The second column in Figure 24 shows the errors in the azimuth and alternate heading, which are primary estimates directly dependent on the path length differences δ_1, δ_2, η_1 and η_2, plotted in the first column. These are plotted as combinations of conventional error histograms and band plots that show the actual spread of the deviations of the estimate from the ground truth reference. These novel band plot representations overcome the quantization effect of histograms caused by binning, and each line represents an actual estimate. The height of the histogram at a given

point can be seen as a function of the unit line density of the corresponding band plot around that point.

As observed from these plots, filtering has clearly different effects on different regions of variation. The deterioration in filtered performance affects the overall error when the sender reaches the sensing limits of the hydrophones on the observer, giving prominence to peaks caused by signals reflected off the tank walls. This results in the error histograms showing more spread than in the unfiltered case. However, there is a marked improvement when peak tracking is enabled. Consequently, the performance of the region between 150 and 250 estimates that is not affected by the aforementioned deterioration actually improves with filtering (Table III).

5.4. Analysis of Results

A large number of experiments were conducted throughout the development process of the relative localization system in two different underwater environments (test tank and lake) with different configurations of the setup in order to evaluate its performance and to gauge the angular and radial sensing range of the system. Aggregate RSE plots of azimuth, heading, alternate heading, range, and alternate range derived from multiple experiments are used in the following sections to analyze the behavior of estimation errors under different experimental conditions.

RSEs of azimuth estimates obtained during five different experiments are plotted in Figure 25. The azimuth was varied as $\theta_0 : -90 \to 0 \to 90$ deg during these tank and lake experiments, which had different initial heading ($\alpha_{\theta=0\,\text{deg}}$) and range ($r_0$) combinations. The RSEs are plotted against the ground truth azimuth for comparison. Table IV lists the means, standard deviations, and average deviations of the errors for the five experiments depicted in Figure 25. The

Table III. Comparison of standard deviations, means, and average deviations of errors associated with azimuth and alternate heading estimates corresponding to the intermediate values plotted in Figure 24.

Variable	No filtering or peak tracking (deg)	Filtered with no peak tracking (deg)	Filtered with peak tracking (deg)
$\sigma_{\Delta\theta}$	20.38 (4.43)	30.06 (2.12)	3.55 (1.79)
$\mu_{\Delta\theta}$	−0.73 (−4.40)	−5.47 (−4.20)	0.04 (−3.91)
$\overline{\Delta\theta}$	11.49 (3.46)	21.46 (1.58)	2.96 (1.43)
$\sigma_{\Delta\acute{\alpha}}$	20.62 (4.41)	30.19 (2.09)	3.54 (1.77)
$\mu_{\Delta\acute{\alpha}}$	0.37 (4.31)	4.50 (3.61)	−0.22 (3.63)
$\overline{\Delta\acute{\alpha}}$	11.57 (3.47)	21.43 (1.56)	2.94 (1.41)

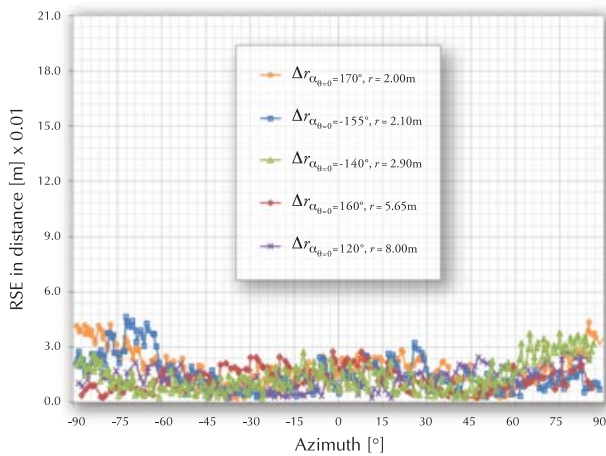The quantities within brackets correspond to the region between estimate numbers 150 and 250.
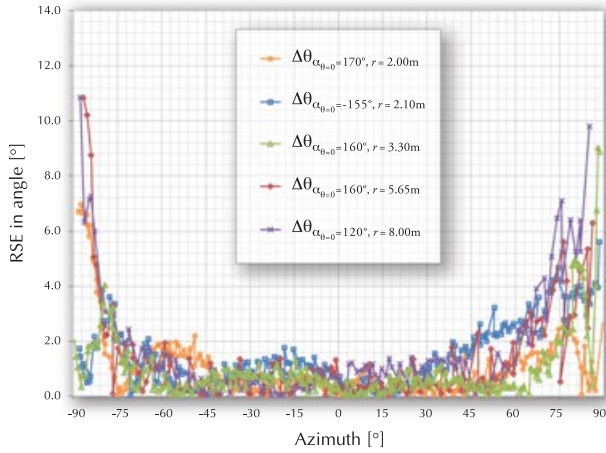
Figure 25. Azimuth estimate errors associated with five azimuth variation experiments with different initial heading and range configurations.

Table IV. Comparison of standard deviations, means, and average deviations of azimuth errors whose RSEs are shown in Figure 25.

Configuration $(\alpha_{\theta=0\ \text{deg}}, r)$	$\sigma_{\Delta\theta}$ (deg)	$\mu_{\Delta\theta}$ (deg)	$\overline{\Delta\theta}$ (deg)
(+170 deg, 2.0 m)	1.63	−0.13	1.02
(−155 deg, 2.1 m)	1.68	+0.05	1.43
(+160 deg, 3.3 m)	1.51	−0.87	0.92
(+160 deg, 6.0 m)	2.25	−0.24	1.30
(+120 deg, 8.0 m)	2.59	−0.15	1.59

consistency of azimuth estimation error behavior across these different experiments becomes evident by observing these tabulated error statistics.

Figure 26 plots range estimate errors associated with five azimuth variation experiments conducted under different conditions. Figure 27 plots range estimate errors associated with five different range variation experiments under different angular configurations in which the range is varied between 5.8 and 10.2 m collectively.

The range error remains invariant as the azimuth and range vary. However, the range estimate errors show a very slight increase as the azimuth approaches ±90 deg,
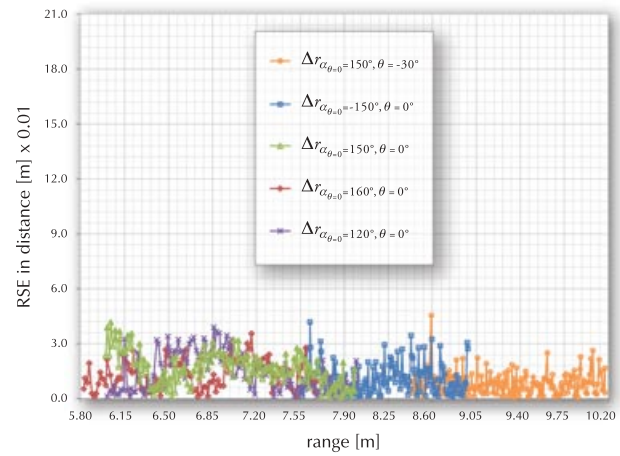
during three (short range) experiments conducted in the test tank, which can be traced to the influence of delayed multipath arrivals of the signal as the source reaches the sensing limits of the receivers. Furthermore, according to Figure 27, the range estimation error slightly *decreases* for the medium-range experiments conducted in the lake compared to the short-range experiments conducted in the test tank. This effect can be attributed to the prevalence of multipath arrivals of the signal in the reverberant environment of the enclosed test tank compared to the lake environment. Table V lists the means, standard deviations, and average deviations of the errors for the five azimuth variation experiments depicted in Figure 26. Table VI lists those quantities corresponding to the five range variation experiments depicted in Figure 27. Inspection of these tabulated values shows the consistency of range estimation error behavior under multiple experimental configurations

Figure 26. Range estimate errors associated with five azimuth variation experiments with different initial heading and range configurations.
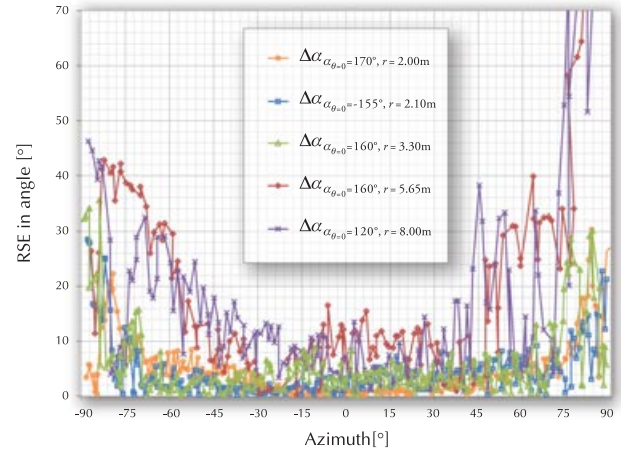

Figure 27. Range estimate errors associated with five range variation experiments with different initial heading and azimuth configurations.

Table V. Comparison of standard deviations, means, and average deviations of range errors whose RSEs are shown in Figure 26.

Configuration $(\alpha_{\theta=0 \text{ deg}}, r)$	$\sigma_{\Delta r}$ $(\times 10^{-3} \text{ m})$	$\mu_{\Delta r}$ $(\times 10^{-3} \text{ m})$	$\overline{\Delta r}$ $(\times 10^{-3} \text{ m})$
(+170 deg, 2.0 m)	21.90	+4.02	19.26
(−155 deg, 2.1 m)	15.27	−11.34	12.06
(−140 deg, 2.9 m)	16.82	+2.87	14.06
(+160 deg, 6.0 m)	12.62	−7.12	10.58
(+120 deg, 8.0 m)	13.85	−3.46	11.93

and environmental conditions. Figure 28 plots the errors associated with heading estimates for five experiments in which the azimuth was varied as $\theta_0 : -90 \rightarrow 0 \rightarrow 90$ deg. These experiments were conducted under different initial headings and ranges both in the test tank and in the lake. Because heading is a secondary estimate calculated using subazimuths and subranges, the performance of heading estimate errors depends on the error performance of azimuth and range estimates as well. Table VII lists the means, standard deviations, and average deviations of the errors for the five experiments depicted in Figure 28.

Figure 29 plots alternate heading estimate errors associated with the five azimuth variation experiments discussed above. The error magnitudes remain invariant with increasing range while increasing only when the azimuth

Figure 28. Heading estimate errors associated with five azimuth variation experiments with different initial heading and range configurations.

approaches ±90 deg. Table VII lists the means, standard deviations, and average deviations of the errors for the five experiments depicted in Figure 29. Inspecting these tabulated values shows that the error performance of the alternate heading estimates remains consistent under different experimental configurations and operational environments.

5.5. System Performance

The performance of the relative localization system is analyzed in terms of accuracy, precision, and sensing limits and how the system recovers from degradation of position estimation accuracy. The following sections will use experimental data obtained from multiple short-, medium-, and long-range experiments presented in this section to evaluate these performance characteristics.

Table VI. Comparison of standard deviations, means, and average deviations of range errors shown in Figure 27.

Configuration $(\alpha_{\theta=0 \text{ deg}}, \theta)$	$\sigma_{\Delta r}$ $(\times 10^{-3} \text{ m})$	$\mu_{\Delta r}$ $(\times 10^{-3} \text{ m})$	$\overline{\Delta r}$ $(\times 10^{-3} \text{ m})$
(+150, −30 deg)	9.82	−0.73	7.71
(−150, 0 deg)	11.39	+6.61	8.76
(+150, 0 deg)	10.85	+14.32	8.47
(−160, 0 deg)	13.95	−6.36	11.18
(+120, 0 deg)	16.11	−6.66	13.76

Table VII. Comparison of standard deviations, means, and average deviations of heading errors shown in Figure 28.

Configuration $(\alpha_{\theta=0 \text{ deg}}, r)$	$\sigma_{\Delta \alpha}$ (deg)	$\mu_{\Delta \alpha}$ (deg)	$\overline{\Delta \alpha}$ (deg)
(+170 deg, 2.0 m)	7.21	+0.74	4.82
(−155 deg, 2.1 m)	7.27	+0.51	4.58
(+160 deg, 3.3 m)	8.91	−0.42	5.57
(+160 deg, 6.0 m)	27.31	−0.63	19.11
(+120 deg, 8.0 m)	26.23	+0.45	17.63

Table VIII. Comparison of standard deviations, means, and average deviations of alternate heading errors shown in Figure 29.

Configuration $(\alpha_{\theta=0 \text{ deg}}, r)$	$\sigma_{\Delta \alpha}$ (deg)	$\mu_{\Delta \alpha}$ (deg)	$\overline{\Delta \alpha}$ (deg)
(+170 deg, 2.0 m)	1.50	−0.33	0.90
(+155 deg, 2.1 m)	1.87	+0.91	1.61
(+160 deg, 3.3 m)	1.65	−0.29	1.10
(+160 deg, 6.0 m)	2.50	−0.06	1.42
(+120 deg, 8.0 m)	2.44	−0.26	1.43
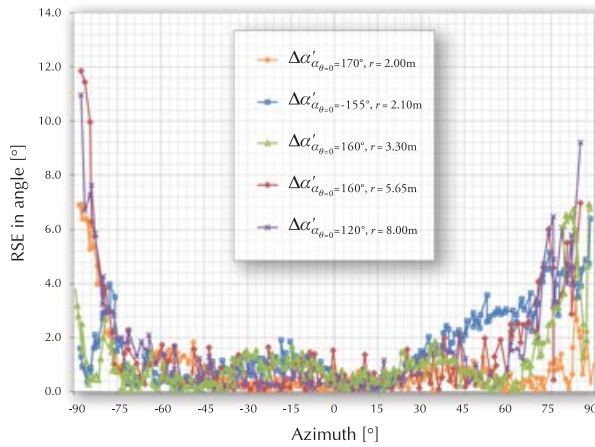
Figure 29. Alternate heading estimate errors associated with five azimuth variation experiments with different initial heading and range configurations.
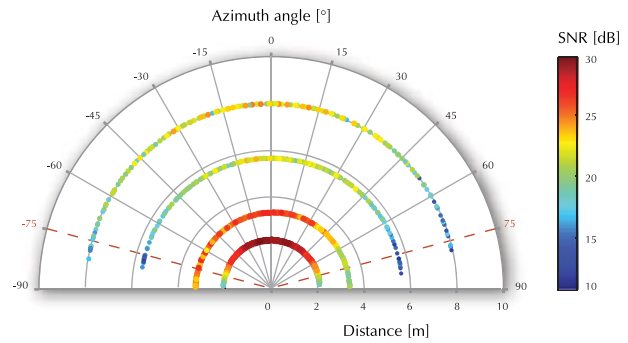

Figure 30. Position estimates produced by four azimuth variation experiments plotted with the color representing the SNR of the received hydrophone channels.

5.5.1. Accuracy and Precision of Estimates

The accuracy and precision of the estimates produced by the relative localization system can be inferred by observing the results and associated errors. The mean and average deviation of error can be considered as performance parameters for each of the different pose vector components.

For all experiments presented, in the test tank as well as in the lake, the mean error for azimuth remained less than 1.0 deg and the average deviations were under 2.0 deg. Estimation errors near the limits of ± 90 deg remained well below 12.0 deg.

For direct estimation of range, the absolute mean error remained below 1.5×10^{-2} m and the average deviation was at most 2.0×10^{-2} m during the presented short-range (test tank) and medium-range (lake) experiments. When considering the long-range experiments, the errors do not warrant direct comparison with the short- and medium-range experiments due to the difference in precision of ground truth references. However, a maximum percentage error defined as [max(avg. dev. of RSE)/max(r_0)] $\times 100$ can be calculated for a series of range estimation experiments. This value is 0.2% for short- and medium-range experiments (up to 10 m of separation between sender and observer) and 0.55% for long-range experiments (up to 90 m of separation between sender and observer).

During all the presented experiments, the mean error for heading estimates remained less than 1.0 deg and the average deviation is under 20.0 deg. Comparatively, the alternate heading estimates were considerably more precise, with a maximum average deviation remaining below 4.0 deg. Estimation errors for alternate heading remained below 12.0 deg in all instances of short- and medium-range experiments.

5.5.2. Angular and Radial Sensing Limits

The angular sensing range (of azimuth estimation) is limited by the directivity of the hydrophones. Although the experiments presented covered the full range of $-90 \rightarrow 90$ deg, the estimation errors, which remained relatively stable below ± 3.0 deg within $-75 \rightarrow 75$ deg, tend to increase beyond that range, as seen from the plot comparison in Figure 25.

Despite the azimuth and range estimation error behavior discussed earlier, the effectiveness of the estimation system deteriorates as the SNR drops. Therefore, as a measure to establish sensing limits of the system, the SNR is calculated for each estimation step. Figure 30 plots the estimated positions with the color representing the calculated SNR at each estimation step. The SNR remains above 10 dB within the angular range $-75 \rightarrow 75$ deg, reaffirming the earlier stated angular sensing limits for the system.

The primary purpose of the long-range experiments was to gauge the maximum radial sensing range of the relative localization system with regard to loss of SNR and deterioration of estimation accuracy. Figure 31 adds position estimates produced by the first segment of a long-range experiment to the previous plots depicted in Figure 30. As seen by the plot, the SNR of received channels drops below 10 dB beyond a range of 75 m. Scattering of the estimated positions beyond a range of 80 m suggests an increase in position error and hence a deterioration of position estimation accuracy. Therefore, the radial sensing limit of the evaluated experimental implementation of the relative localization system can be stated as 75 m, within which sufficiently accurate position estimates are produced (i.e., where azimuth error remains below ± 3.0 deg).

5.5.3. System Recovery

Azimuth and range estimates obtained during the full 15-min duration of a long-range experiment are plotted along with measured SNR in Figure 32. The SNR continues to
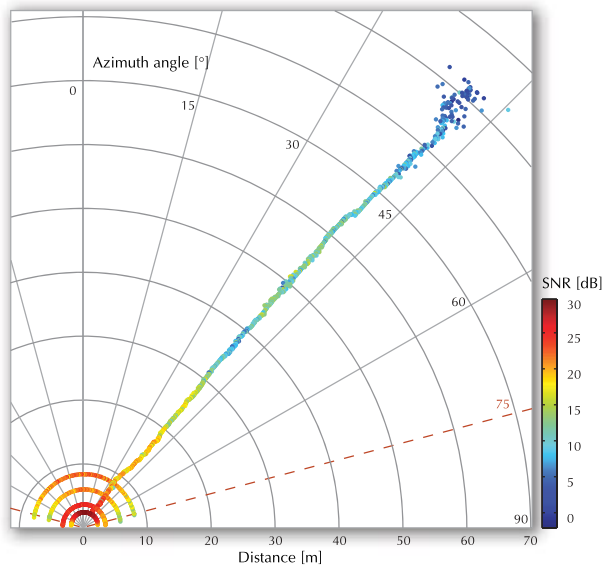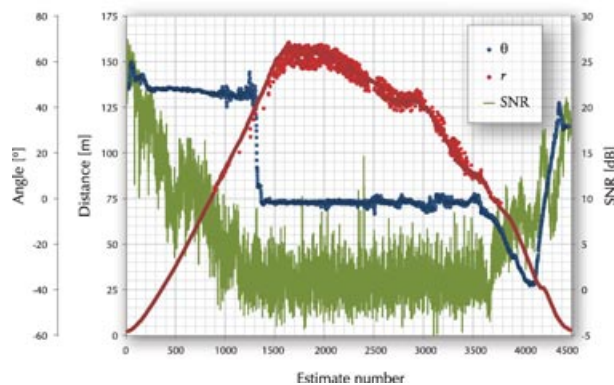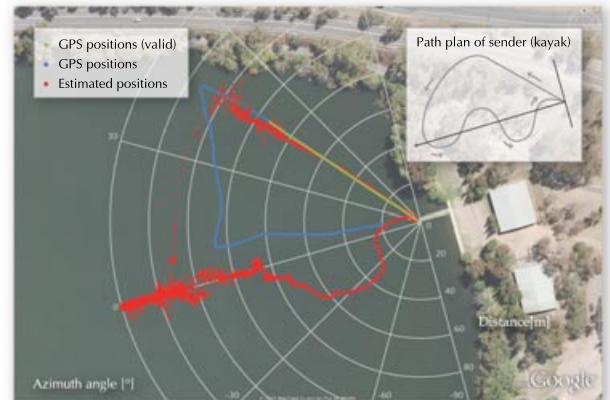
Figure 31. Position estimates produced by the first segment of a long-range experiment and four azimuth variation experiments plotted with the color representing the SNR of the received hydrophone channels.

Figure 33. Estimated sender positions obtained during a long-range experiment plotted with the GPS "ground truth" track and the path plan of the sender. The "valid" segment of the GPS track used for ground truth–based error calculations is shown in green. The GPS coordinates of the pole (position of the observer) of the coordinate system are 35 deg 17′ 10″ S, 149 deg 5′ 58″ E. The polar axis has a 13 deg counterclockwise rotation from true north. (Background image courtesy Google, © 2009 MapData Science Pty Ltd.)

drop with increasing range and drops below 0 dB as the range estimates reach 125 m. For the first segment of the same experiment, it was shown earlier that position errors start to increase as the SNR drops below 10 dB, which corresponds to a range of approximately 75 m.

Even as the SNR drops below 0 dB intermittently up to about estimate number 1300, the azimuth estimates remain relatively stable due to peak tracking. However, as the SNR further deteriorates beyond estimate number 1300, the azimuth estimation gradually approaches 0 deg as the

cross correlograms used for TDOA estimation return a peak corresponding to the weakly correlated ambient noise instead of the weak signal. The gradual approach instead of an abrupt change is due to peak tracking, which attempts to maintain a trend in peak positions based on the current and previous estimates. The range estimate errors are bounded by a combination of peak tracking and range tracking ($N_{RT} = 768$, corresponding to a spatial window length of 10 m). The range estimation is unaffected by correlated ambient noise and will return random errors within the bounds defined by the channel window size when the signal is no longer producing a discernible peak in the cross-correlogram output by matched filter processing. Additionally, unlike the azimuth estimation, the range estimation responds quickly when the SNR improves even for a few estimates as seen by the plot—especially near estimate number 2500. When the range decreased (kayak/sender approaching the pier/observer), causing the SNR to increase beyond 0 dB, both the azimuth and range estimates regained accuracy and continued to track the path of the sender. This "self-recovery" is facilitated by appropriate selection of the tolerance parameter for the peak tracking scheme. The track of the kayak/sender relative to the observer, consisting of positions estimated at a rate of 5.0 Hz during this long-range experiment, is plotted in Figure 33 against a background image showing the actual location of the experiment at Lake Burley Griffin. The gradual "wandering" of the estimated track due to the azimuth estimate approaching 0 deg can be seen in this plot. Only a segment

Figure 32. Azimuth and range estimates obtained during the full duration of the long-range experiment plotted with the corresponding SNR of received hydrophone channels at each estimation step.

of the GPS track[25] up to a range of 95 m was used as the ground truth.

6. CONCLUSIONS

To address the localization requirements of Serafina-class AUVs to operate as a swarm, a fully decentralized relative localization system comprising a *localization sensor* capable of producing instantaneous estimates of relative azimuth, range, and heading of neighboring AUVs was developed and experimentally evaluated. The choice of a short-duration, acoustically transmitted MLS ping as the source signal helped to mitigate some of the detrimental characteristics of the underwater acoustic channel. Its statistical properties led to better cross-correlation performance in the presence of multipath propagation and interference compared to other candidate pseudo noise signals and chirps (Kottege, 2009). The azimuth estimations were done using hyperbolic localization methods, and the heading estimate was derived from the intermediate angular and radial measurements. In addition, an alternate method utilizing a reverse hyperbolic localization scheme based on transducer geometry was used to calculate the heading and range independent of the earlier estimations, adding redundancy to the position estimation and improving reliability.

The relative localization strategy proposed and presented in this article represents a novel approach that has no precedent in the surveyed underwater robotics literature. Moreover, the position estimates produced by the relative localization system demonstrate a higher degree of accuracy and precision when compared to the state of the art in addressing the problem of localization for multiple-AUV navigation (compared to systems summarized in Table I). This is especially significant when considering the higher update rates, low cost, small size, and fully decentralized and distributed implementation possibilities of the system in the context of the small and agile Serafina-class AUVs that motivated the research.

Although the requirements and constraints were derived based on the concept of swarming Serafina-class AUVs, the relative localization methodology and innovative strategies developed throughout this article can be used in many other underwater applications, which are not limited to small AUV swarms (e.g., underwater sensor network localization, tracking of aquatic fauna). The experimental results and analyses that were presented herein contribute to the growing field of acoustic localization in the context of understanding limitations and opportunities presented by underwater environments.

---

[25]GPS positions received beyond 300 s of initiating the experiment were affected by large drifts (Wing, Eklund, & Kellogg, 2005). Therefore, the "ground truth" reference beyond that was deemed unreliable.

REFERENCES

Arulampalam, M. S., Ristic, B., Gordon, N. J., & Mansell, T. (2004). Bearings-only tracking of manoeuvring targets using particle filters. EURASIP Journal on Applied Signal Processing, 2004(15), 2351–2365.

Bahr, A. (2009). Cooperative localization for autonomous underwater vehicles. Ph.D. thesis, MIT, Cambridge, MA.

Baker, B. N., Odell, D. L., Anderson, M. J., Bean, T. A., & Edwards, D. B. (2005, August). Performance of a two-hydrophone heading sensor and AUV formation flying controller. In International Symposium on Unmanned Untethered Submersible Technology 2005 (UUST '05), Durham, NH.

Bar-Shalom, Y., Kirubarajan, T., & Li, X.-R. (2002). Estimation with applications to tracking and navigation. New York: Wiley.

Bellingham, J. C., Consi, T. R., Tedrow, U., & Di, D. (1992, June). Hyperbolic acoustic navigation for underwater vehicles: Implementation and demonstration. In Proceedings of IEEE Symposium on Autonomous Underwater Vehicle Technology, Washington, DC.

Borish, J., & Angell, J. B. (1983). An efficient algorithm for measuring the impulse response using pseudo-random noise. Journal of the Audio Engineering Society, 31(7), 478–488.

Corke, P., Detweiler, C., Dunbabin, M., Hamilton, M., Rus, D., & Vasilescu, J. (2007, April). Experiments with underwater robot localization and tracking. In Proceedings of IEEE International Conference on Robotics and Automation (ICRA 2007), Rome, Italy (pp. 4556–4561).

Cruz, N., Madureira, L., Matos, A., & Pereira, F. L. (2001, November). A versatile acoustic beacon for navigation and remote tracking of multiple underwater vehicles. In MTS/IEEE Oceans 2001, Honolulu, HI (pp. 1829–1834).

Curcio, J., Leonard, J., Vaganay, J., Patrikalakis, A., Bahr, A., Battle, D., Schmidt, H., & Grund, M. (2005, September). Experiments in moving baseline navigation using autonomous surface craft. In Proceedings of IEEE/MTS Oceans 2005, Washington, DC (pp. 730–735).

Davis, R., Leonard, N., & Frantantoni, D. (2009). Routing strategies for underwater gliders. Deep-Sea Research II: Topical Studies in Oceanography, 56(3–5), 173–187.

Deffenbaugh, M., Bellingham, J. G., & Schmidt, H. (1996, September). The relationship between spherical and hyperbolic positioning. In Proceedings of MTS/IEEE Oceans 1996, Fort Lauderdale, FL.

Eustice, R. M., Whitcomb, L. L., Singh, H., & Grund, M. (2007, April). Experimental results in synchronous-clock one-way-travel-time acoustic navigation for autonomous underwater vehicles. In Proceedings of IEEE International Conference on Robotics and Automation (ICRA 2007), Rome, Italy (pp. 4257–4264).

Farina, A. (1998, September). MLS impulse response measurements for underwater bottom profiling. In Proceedings of the 4th European Conference on Underwater Acoustics (ECUA), Rome, Italy (pp. 21–25).

Fiorelli, E., Leonard, N. E., Bhatta, P., Paley, D. A., Bachmayer, R., & Fratantoni, D. M. (2006). Multi-AUV control and

adaptive sampling in Monterey Bay. IEEE Journal of Oceanic Engineering, 31(4), 935–948.

Fox, D., Burgard, W., Kruppa, H., & Thrun, S. (2000). A probabilistic approach to collaborative multi-robot localization. Autonomous Robots, 8(3), 325–344.

Freitag, L., Grund, M., Singh, I., Partan, J., Koski, P., & Ball, K. (2005, September). The WHOI Micro-Modem: An acoustic communications and navigation system for multiple platforms. In Proceedings MTS/IEEE Oceans 2005, Brest, France.

Golomb, S. W. (1982). Shift register sequences, rev. ed Laguna Hills, CA: Aegean Park Press.

Gordon, N. J., Salmond, D. J., & Smith, A. F. M. (1993). Novel approach to nonlinear/non-Gaussian Bayesian state estimation. IEE Proceedings-F, Radar and Signal Processing, 140(2), 107–113.

Hermand, J.-P., & Roderick, W. I. (1993). Acoustic model-based matched filter processing for fading time-dispersive ocean channels: Theory and experiment. IEEE Journal of Oceanic Engineering, 18(4), 447–465.

Hoe, A. (2002). Adamt19937. http://adrianhoe.com/adrianhoe/projects/adamt19937/. Accessed January 10, 2010.

Howard, A., Mataric, M. J., & Sukhatme, G. S. (2003, March). Cooperative relative localization for mobile robot teams: An ego-centric approach. In Proceedings from the International Workshop on Multi-Robot Systems, Washington, DC (pp. 65–76).

Kalantar, S., & Zimmer, U. R. (2009). Optima localization by vehicle formations imitating the Nelder–Mead simplex algorithm. Autonomous Robots, 27(3), 239–260.

Knapp, C., & Carter, G. (1976). The generalized correlation method for estimation of time delay. IEEE Transactions on Acoustics, Speech, and Signal Processing, 24(4), 320–327.

Kottege, N. (2009). Underwater acoustic localisation in the context of autonomous submersibles. Ph.D. thesis, The Australian National University, Canberra, ACT, Australia.

Kottege, N., & Zimmer, U. R. (2007, April). Relative localization for AUV swarms. In Proceedings of the International Symposium on Underwater Technology (UT '07), Tokyo, Japan (pp. 588–593).

Kottege, N., & Zimmer, U. R. (2008a, December). Cross-correlation tracking for maximum length sequence based acoustic localisation. In Proceedings of the Australasian Conference on Robotics and Automation (ACRA 2008), Canberra, ACT, Australia.

Kottege, N., & Zimmer, U. R. (2008b). MLS-based, distributed bearing, range, and posture estimation for schools of submersibles. Experimental Robotics (pp. 377–385). Berlin: Springer.

Lamport, L. (1978). Time, clocks, and the ordering of events in a distributed system. Communications of the ACM, 21(7), 558–565.

Leonard, J. J., & Durrant-Whyte, H. F. (1991). Mobile robot localization by tracking geometric beacons. IEEE Transactions on Robotics and Automation, 7(3), 376–382.

Matsumoto, M., & Nishimura, T. (1998). Mersenne twister: A 623-dimensionally equidistributed uniform pseudorandom number generator. ACM Transactions on Modeling and Computer Simulation, 8(1), 3–30.

Olson, E., Leonard, J., & Teller, S. (2006). Robust range-only beacon localization. IEEE Journal of Oceanic Engineering, 31(4), 949–958.

Olson, E., Leonard, J. J., & Teller, S. (2004, June). Robust range-only beacon localization. In IEEE/OES Autonomous Underwater Vehicles 2004, Sebasco, ME (pp. 66–75).

Piersol, A. G. (1981). Time delay estimation using phase data. IEEE Transactions on Acoustics, Speech, and Signal Processing, 29(3), 471–477.

Ristic, B., Arulampalam, S., & McCarthy, J. (2002). Target motion analysis using range-only measurements: Algorithms, performance and application to ISAR data. Signal Processing, 82(2), 273–296.

Schill, F. (2007). Distributed communication in swarms of autonomous underwater vehicles. Ph.D. thesis, The Australian National University, Canberra, ACT, Australia.

Schill, F., & Zimmer, U. R. (2006). Distributed dynamical omnicast routing. Complex Systems, 16(4), 299–316.

Schill, F., & Zimmer, U. R. (2007, April). Pruning local schedules for efficient swarm communication. In Proceedings of the International Symposium on Underwater Technology (UT '07), Tokyo, Japan (pp. 594–600).

Schill, F., Zimmer, U. R., & Trumpf, J. (2005, September). Towards optimal TDMA scheduling for robotic swarm communication. In Proceedings of Towards Autonomous Robotic Systems (TAROS 2005), London, UK.

Somaraju, R., & Schill, F. (2007). A communication module and TDMA scheduling for a swarm of small submarines. Turkish Journal of Electrical Engineering & Computer Sciences, 15(2), 283–306.

Stojanovic, M., Freitag, L., Leonard, J. J., & Newman, P. (2002, October). A network protocol for multiple AUV localization. In MTS/IEEE Oceans 2002, Biloxi, MI (pp. 604–611).

Thrun, S., Fox, D., Burgard, W., & Dellaert, F. (2001). Robust Monte Carlo localization for mobile robots. Artificial Intelligence, 128(1–2), 99–141.

Turin, G. L. (1960). An introduction to matched filters. IRE Transactions on Information Theory, 6(3), 311–329.

Urick, R. J. (1983). Principles of underwater sound. New York: McGraw-Hill.

Ward, D. B., Lehmann, E. A., & Williamson, R. C. (2003). Particle filtering algorithms for tracking an acoustic source in a reverberant environment. IEEE Transactions on Speech and Audio Processing, 11(6), 826–836.

Wing, M. G., Eklund, A., & Kellogg, L. D. (2005). Consumer-grade global positioning system (GPS) accuracy and reliability. Journal of Forestry, 103(4), 169–173.